6546–6571 *Nucleic Acids Research, 2017, Vol. 45, No. 11* *Published online 8 May 2017*
doi: 10.1093/nar/gkx392

PRL-3 promotes telomere deprotection and chromosomal instability

Shenyi Lian[1,2,*,†], Lin Meng[1,†], Yongyong Yang[1,†], Ting Ma[1,†], Xiaofang Xing[1], Qin Feng[3], Qian Song[1], Caiyun Liu[1], Zhihua Tian[3], Like Qu[1,*] and Chengchao Shou[1,*]

[1]Key Laboratory of Carcinogenesis and Translational Research (Ministry of Education), Department of Biochemistry and Molecular Biology, Peking University Cancer Hospital & Institute, Beijing 100142, China, [2]Department of Pathology, Peking University Cancer Hospital & Institute, Beijing 100142, China and [3]Central Laboratory, Peking University Cancer Hospital & Institute, Beijing 100142, China

Received May 12, 2016; Revised April 19, 2017; Editorial Decision April 25, 2017; Accepted April 26, 2017

ABSTRACT

Phosphatase of regenerating liver (PRL-3) promotes cell invasiveness, but its role in genomic integrity remains unknown. We report here that shelterin component RAP1 mediates association between PRL-3 and TRF2. In addition, TRF2 and RAP1 assist recruitment of PRL-3 to telomeric DNA. Silencing of PRL-3 in colon cancer cells does not affect telomere integrity or chromosomal stability, but induces reactive oxygen species-dependent DNA damage response and senescence. However, overexpression of PRL-3 in colon cancer cells and primary fibroblasts promotes structural abnormalities of telomeres, telomere deprotection, DNA damage response, chromosomal instability and senescence. Furthermore, PRL-3 dissociates RAP1 and TRF2 from telomeric DNA *in vitro* and in cells. PRL-3-promoted telomere deprotection, DNA damage response and senescence are counteracted by disruption of PRL-3–RAP1 complex or expression of ectopic TRF2. Examination of clinical samples showed that PRL-3 status positively correlates with telomere deprotection and senescence. PRL-3 transgenic mice exhibit hallmarks of telomere deprotection and senescence and are susceptible to dextran sodium sulfate-induced colon malignancy. Our results uncover a novel role of PRL-3 in tumor development through its adverse impact on telomere homeostasis.

INTRODUCTION

The phosphatase of regenerating liver (PRL) family includes PRL-1, PRL-2 and PRL-3, which emerges as potential biomarkers for various types of cancer (1–3). Reports from several groups highlight the role of PRL-3 in promoting cancer metastasis through enhanced cell motility and invasiveness (1,3), and further studies reveal that PRL-1 and PRL-2 have similar effects (2–5). As a phosphatase, only few phosphorylated proteins were identified as substrates of PRL-3 (6–8). Instead, PRL-3 could activate Rho-family GTPases, EGFR, PI3K-AKT, MAPK, STAT3/5, NF-κB and mTOR (1,3,9–12). Tyrosine phosphoproteome analysis identified PRL-3 as a nexus of pro-invasive signal networks (13). Recently, antibody array-based screening disclosed PRL-3′s potential to activate both tyrosine and serine/threonine phosphorylations of diverse signaling proteins (14). PRL-3 also modulates gene transcription through the functional and/or physical associations with key transcriptional factors (10,15–17). Moreover, the role of PRL-3 in epigenetic regulation was proposed, but the mechanism is unclear (18,19). In *Xenopus laevis*, lose-of-function and gain-of-function studies showed that PRL-3 is required for migration of cephalic neural crest cells during embryonic development (20). The PRL-3-null mice develop 50% less tumors in an experimental model of colitis-associated colon cancer (21). A subsequent study further showed that colitis-associated cancer cells isolated from PRL-3-null mice had reduced clonogenicity and tumor-initiation capacity, underscoring the stimulatory role of PRL-3 in tumorigenesis (22). Despite of relatively low expression in normal tissues and untransformed cells, high expression of PRL-3 was frequently found in cancer tissues (1,3,23). Thus, it is also critical to evaluate the role of PRL-3 gain-of-function in tumorigenesis with model systems.

Tumorigenesis is a dynamic process driven by oncogenic activation (24). In addition to promoting cell proliferation and enhancing invasiveness, activated oncogenes can destabilize chromosomal structures and generate DNA double-strand breaks (DSBs) (25–27). Elevated DSBs and

*To whom correspondence should be addressed. Tel: +86 10 8819 6766; Fax: +86 10 8812 2437; Email: cshou@vip.sina.com
Correspondence may also be addressed to Like Qu. Tel: +86 10 8819 6769; Fax: +86 10 8812 2437; Email: qulike@bjcancer.org
Correspondence may also be addressed to Shenyi Lian. Tel: +86 10 8819 6769; Fax: +86 10 8812 2437; Email: liansy@bjmu.edu.cn
†These authors contributed equally to the paper as first authors.

increased DNA damage response (DDR) were documented in human precancerous lesions and cancers, which may set a barrier against the tumorigenesis through oncogene-induced senescence (25–27). However, these may also initiate senescence-associated secretory phenotype and favor the selection for cells defective in DDR, resulting in malignant transformation (27–29).

Integrity of telomeres is required for maintaining the chromosomal stability and counteracting tumor development (30,31). Repair of functional and dysfunctional telomeres is orchestrated by telomerase, shelterin and several other key factors (31). Shelterin components, including TRF1, TRF2, RAP1, POT1, TIN2 and TPP1, cooperatively safeguard telomeric DNA from damage (31,32), and also possess unique extra-telomeric functions (33–36). Telomeric Repeat-binding Factor 2 (TRF2) binds to telomere repeats ($[TTAGGG]_n$) through homodimerization (37) and participates in telomere loop formation (38). TRF2 physically interacts with ATM kinase and inhibits ATM-dependent DDR (39). In addition, TRF2 is essential for repressing classical Ku70/80- and Ligase IV-dependent non-homologous end joining (NHEJ) repair of telomeres to prevent chromosome fusions (38, 40–43). Repressor Activator Protein 1 (RAP1) was initially identified from *Saccharomyces cerevisiae*, and is essential for telomere length control and telomere end protection against NHEJ-mediated repair pathway (44). Unlike yeast RAP1, which can interact with telomeric DNA through its Myb domain, mammalian RAP1 is recruited to telomeres in a TRF2-dependent manner (45). At present, the role of mammalian RAP1 in telomere end protection remains controversial. In human cells with RAP1 knocked out, telomeres were still protected from NHEJ and homology directed repair (HDR) (46). On the other hand, RAP1 was shown to inhibit NHEJ independently of TRF2 (47). Deletion of RAP1 in mice generated no obvious effects on the telomere length or animal viability (48, 49), but accelerated HDR in the context of Ku70/80 deficiency (49). Removal of RAP1 from telomeric DNA by disrupting TRF2–RAP1 interaction can also induce aberrant HDR in mouse embryonic fibroblasts (50). Mice deficient for both RAP1 and telomerase exhibited pronounced telomere shortening and DDR (51). Moreover, RAP1 could cooperate with the basic domain of TRF2 to repress telomere loadings of PARP1 and SLX4, thereby preventing inappropriate processing of telomeres by the HDR pathway (52). Recently, RAP1 was shown to prevent NHEJ when DNA condensation-mediated telomere protection is impaired (53).

Telomere deprotection is one of key factors for tumor development in human (30,54,55). Dysfunctional telomere due to excessive deprotection induces persistent DDR and senescence (56–59). Telomere dysfunction-induced senescence could hinder tumor growth in the animal model (60), but checkpoint deregulation by introducing active telomerase or inhibiting key signaling factors could override senescence and was predicted to facilitate tumorigenesis (57,61–63). In this study, we present evidence that overexpression of PRL-3 elicits structural abnormalities in telomeres, telomere dysfunction, telomere deprotection, DNA damage response, chromosomal instability and senescence. Mechanistically, PRL-3 has a capacity to dissociate RAP1 and TRF2 from telomeric DNA. In addition, telomere deprotection and senescence are associated with PRL-3-promoted colon tumorigenesis in a transgenic mouse model.

MATERIALS AND METHODS

Cell lines, plasmids, small Interference RNAs (siRNAs), short hairpin RNAs (shRNAs) and single-guide RNA (sgRNA)

The human colon cancer cell lines HCT116, LoVo, DLD-1 and SW480, breast cancer cell lines MDA-MB-231 and MCF-7, lung cancer cell line H460 and African green monkey kidney cell line COS7 were obtained from ATCC. Primary human fibroblasts IMR90 (PD15) and WI38 (PD20) were obtained from Cell Center, Chinese Academy of Medical Science (Beijing, China).

Full-length human *PRL3* gene was cloned from a LoVo cDNA library and inserted into the pcDNA3 vector. Indicated amount of plasmids was transiently transfected into cells cultured in 60 mm plates with Lipofectamine 2000 reagent (Thermo Fisher Scientific).

For transient knockdown of PRL-3, following siRNAs (synthesized by GenePharma, Shanghai, China) were used: PRL-3 #1, sense: 5′-ACAAACACAUGCGCUUCCUdTdT-3′, antisense: 5′-AGGAAGCGCAUGUGUUUGUdTdT-3′; PRL-3 #2, sense: 5′-UUGAGGACCUGAAGAAGUAdTdT-3′, antisense: 5′-UACUUCUUCAGGUCCUCAAdTdT-3′; PRL-3 #3, sense: 5′-CAGCUCCUGUGUGGAGAAAdTdT-3′, antisense: 5′-UUUCUCCACACAGGAGCUGdTdT-3′; PRL-3 #4, sense: 5′-GACCAGAUGCUCAUGUGUUdTdT-3′, antisense: 5′-AACACAUGAGCAUCUGGUCdTdT-3′; control, sense: 5′-UUUUCCGAACGUGUCACGUdTdT-3′, antisense: 5′-ACGUGACACGUUCGGAAAAdTdT-3′. siRNA pools specific for RAP1 (SR 310061) and TRF2 (SR304782) were obtained from OriGene. siRNAs (50 nM) were transfected into cells cultured in 60 mm plates with Lipofectamine 2000 reagent.

HCT116 and LoVo cells stably expressing PRL-3 and control cells were established previously (10,11). To stably express PRL-3 in primary fibroblast, WI38 cells were infected with 50 MOI control or PRL-3-expressing lentivirus for 96 h. To express ectopic TRF2, HCT116 cells were infected with 100 MOI control or TRF2-expressing lentivirus for 120 h. Stable knockdown of PRL-3 in HCT116 cells was achieved by lentivirus-mediated transduction of shRNAs against two sequences of PRL-3: 5′-CCCAGCTCCTGTGTGGAGAAAG-3′ (PRL-3 #3) and 5′-GACCAGATGCTCATGTGTTCC-3′ (PRL-3 #4). Control shRNA sequence was 5′-TTCTCCGAACGTGTCACGTTT-3′. All Lentiviral vectors were provided by GenePharma. To generate SW480 cells knockout (KO) for PRL-3, CRISPR/Cas9-mediated *PRL3* gene editing was performed by ViewSolid Biotech (Beijing, China). PRL-3-specific sgRNA (5′-AGGACCTGAAGAAGTACGGGG-3′) was cloned into VK001-004 vector (pCAG-T7-Cas9-gRNA-Pgk-Puro-T2A-mCherry). SW480 cells were transfected with sgRPL-3-expressing vector with Lipofectamine 2000. After sorting of mCherry positive cells by flow cytometry, cells were seeded into 96-well plates and selected with 2 μg/ml

puromycin (Thermo Fisher Scientific) for 4 weeks. Independent monoclones were genotyped to verify successful targeting.

Antibodies and reagents

Mouse anti-PRL-3 monoclonal antibody (clone 4G8) was generated by immunizing mice with KLH-conjugated full-length human PRL-3 following standard protocols. Commercially obtained primary antibodies included: anti-RAP1 (A300-306A-2) was from Bethyl; anti-TRF2 (OP129) was from Calbiochem; anti-TRF2 (ab4182), anti-TIN2 (ab59B388), anti-POT1 (ab21382), anti-TPP1 (ab5759), anti-H3K9me3 (ab8898), anti-Ku70 (ab3114), anti-Ku80 (ab119935) and anti-Histone 2B (Ab18977) were from Abcam; anti-β-tubulin (sc-9104), anti-p53 (sc-126), anti-p65 (sc-372) and anti-RAD51 (sc-8349) were from Santa Cruz; anti-TRF1 (NBP1-00663) was from Novus; anti-γH2AX (20E3), anti-pERK1/2 (9106), anti-cyclin D1 (2978), anti-pSer1981-ATM (4526), anti-pSer345-CHK1 (2348), anti-pT68-CHK2 (2661), anti-pS536-p65 (3033), anti-pS1981-ATM (10H11), and anti-pSer10-H3 (9706) were from Cell Signaling; anti-BrdU (555627) was from BD; anti-cleaved caspase-3 (AC033) was from Beyotime (Beijing, China); anti-53BP1 (BS1714) was from Bioworld; anti-GAPDH (10494-1-AP) was from Proteintech; anti-myc-tag (AB103) and anti-GST-tag (AB101) were from TianGen (Beijing, China). HRP-anti-mouse (ab6789), HRP-anti-rabbit (ab6721), HRP-Protein A (ab7456), TRITC-anti-mouse (ab6786), TRITC-anti-rabbit (ab6718), FITC-anti-mouse (ab6785) and FITC-anti-rabbit (ab97050) were obtained from Abcam and used as secondary antibodies. Benzonase, thymidine, doxycycline (DOX), RNase A, colcemid, Bromodeoxyuridine (BrdU), bromodeoxycytidine (BrdC) and aphidicolin were from Sigma. KU55933 was from Santa Cruz. Dextran sodium sulfate (DSS) was from MP Biomedicals.

Recombinant proteins and *in vitro* binding assays

Recombinant FLAG-TRF2, myc-TRF2 and myc-PRL-3 (all from OriGene) were expressed in human HEK293 cells and purified. Full-length human *TRF2* gene was cloned from a HCT116 cDNA library and inserted into pGEX4T1 vector. His-tagged human PRL-3 was reported previously (10). Full-length human *RAP1* gene was cloned from a LoVo cDNA library, and *RAP1* deletion mutants were generated by polymerase chain reaction (PCR) and inserted into the pGEX4T1 expression vector. Truncated forms of GST-RAP1 included: Myb domain (Myb, amino acids 128–188), deletion of BRCT domain (ΔB, amino acids 102–399), deletion of BRCT and Myb domains (ΔBΔM, amino acids 189–399), deletion of NLS domain (ΔN, amino acids 1–382) and deletion of Coiled-coil, RCT and NLS domains (ΔCΔRΔN, amino acids 1–188). His-tagged human RAP1 was constructed by inserting the *RAP1* cDNA into pET-28a vector. GST-tagged and His-tagged recombinant proteins were expressed in BL21 (DE3) bacteria and respectively purified with glutathione-Sepharose and Ni-NTA agarose beads (all from Thermo Fisher Scientific).

For *invitro* GST pull-down or FLAG pull-down assay, 100 ng of the indicated purified proteins were co-incubated in 500 μl binding buffer I (50 mM Tris–HCl pH 7.9, 150 mM NaCl, 1% Triton X-100, 2 mM DTT, 0.1 mM PMSF, 5% glycerol) for 3 h at 4°C. Where indicated, mixtures of purified protein were pre-treated with benzonase nuclease (250 units) for 30 min at room temperature. Next, 30 μl glutathione-Sepharose or anti-FLAG agarose (OriGene) beads were added and co-incubated for 1 h at 4°C. The beads were collected by centrifugation at 5000 rpm at 4°C for 10 min, washed five times with binding buffer I, eluted by boiling in 2× loading buffer, and analyzed by western blot. Alternatively, to precipitate PRL-3-binding shelterin proteins, HCT116 cells were homogenized in ice-cold lysis buffer containing 50 mM Tris–HCl pH 7.4, 300 mM NaCl, 50 mM NaF, 1 mM EDTA, 1 mM DTT, 1% Triton X-100, 10% glycerol and 1× protease inhibitor cocktail from Roche. After centrifugation at 12 000 rpm for 15 min at 4°C, the supernatant (500 μg) was co-incubated with 1 μg purified GST-PRL-3 or GST, plus 30 μl glutathione-Sepharose beads for 12 h at 4°C. The beads were collected by centrifugation at 1000 rpm at 4°C for 10 min, washed five times with lysis buffer, eluted by boiling in 2× loading buffer and analyzed by western blot.

For the *invitro* DNA–protein binding assay, 20 μl streptavidin agarose beads (Thermo Fisher Scientific) were pre-incubated with 1 μg biotin-$[TTAGGG]_3$ or biotin-Alu (5′-CGGGAAGCAGAGGTTGTAGTGAGCC-3′, corresponding to the 3′-end of the Alu repeat element) duplex DNA (both synthesized by SBS Genetech, Shanghai, China) in 500 μl binding buffer II (50 mM Tris–HCl pH 7.9, 150 mM NaCl, 1% Triton X-100, 1 mM DTT, 0.1 mM PMSF, 1% BSA, 5% glycerol) for 2 h at room temperature, followed by addition of purified myc-TRF2 (150 ng), His-RAP1 (120 ng) and His-PRL-3 (30 ng). After co-incubation at 4°C for 4 h, the precipitates were collected by centrifugation at 1000 rpm at 4°C for 10 min, washed four times with binding buffer II, twice with phosphate buffered saline (PBS), eluted in 2× loading buffer and analyzed by western blot.

EMSA (electrophoretic mobility shift assay)

EMSA (electrophoretic mobility shift assay) was performed by using LightShift Chemiluminescent EMSA Kit (Thermo Fisher Scientific). In brief, 20 nM of biotin-$[TTAGGG]_{12}$ (SBS Genetech) was co-incubated with indicated concentrations of purified FLAG-TRF2, His-RAP1 and myc-PRL-3 in 10 μl binding buffer III (10 mM Tris–HCl pH 7.5, 50 mM KCl, 1 mM DDT, 1 μg poly dI-dC, 2.5% glycerol, 5 mM $MgCl_2$) for 25 min at room temperature. Where indicated, 0.1 μg antibody to PRL-3, TRF2 or pre-immune IgG was added 15 min before termination of the reaction. Ficoll was added (3% final w/v) and the samples were loaded on the 6% polyacrylamide 0.5× Tris-broate-EDTA (TBE) gel (29:1, Acry:Bisacry). Gel was run at 4.5 V/cm in 0.5× TBE at 4°C for 90 min, followed by transfer to polyvinylidene difluoride membrane. After crosslinking with Stratalinker 1800 (Stratagene) at Auto-crosslink mode, the membrane was probed with HRP-conjugated streptavidin solution at room temperature for 45 min. The protein–DNA complex was visualized by using HRP Substrate Working Solution.

Subcellular fractionation

To make cytoplasmic and nuclear extracts, cells at 80% confluence were homogenized in ice-cold Buffer A (10 mM HEPES pH 7.9, 10 mM KCl, 0.1 mM EDTA, 1 mM DTT and 1× protease inhibitor cocktail) on ice for 20 min, then supplemented with NP-40 to 0.5% (v/v), vortexed, incubated for another 10 min and centrifuged at 1500 *g* for 5 min at 4°C. The supernatants were re-centrifuged at 13 000 *g* for 15 min at 4°C to obtain the cytoplasmic extracts. The pellets (nuclei) were washed twice with Buffer A and directly homogenized in 2× loading buffer to obtain the whole nuclear extracts. Alternatively, after being washed with Buffer A for two times, the nuclei were homogenized in ice-cold Buffer B (20 mM HEPES pH 7.9, 1 mM EDTA, 10 mM NaF, 2 mM DTT, 1% Triton X-100, 10% glycerol and 1× protease inhibitor cocktail) containing 400 mM NaCl for 30 min and centrifuged at 18 000 *g* for 30 min at 4°C to obtain nucleoplasmic fractions. The pellets were washed twice with Buffer B and homogenized in 2× loading buffer to obtain the chromatin-enriched fractions. For sequential extraction of chromatin-enriched fractions, the nuclei were homogenized in ice-cold Buffer B containing 150 mM, 300 mM, 500 mM, and 700 mM NaCl.

Western blot and immunoprecipitation

Cells were directly homogenized in 2× loading buffer to prepare whole cell extracts. Human colon cancer tissues (provided by the Tissue Bank of Peking University Cancer Hospital & Institute, Beijing, China) and mouse tissues were homogenized in RIPA buffer containing 50 mM Tris–HCl pH 7.4, 150 mM NaCl, 50 mM NaF, 1 mM EDTA, 1 mM DTT, 1% Triton X-100, 0.1% sodium dodecyl sulphate (SDS) and 1× protease inhibitor cocktail. For immunoprecipitation, cells were homogenized in ice-cold lysis buffer containing 50 mM Tris–HCl pH 7.4, 300 mM NaCl, 50 mM NaF, 1 mM EDTA, 1 mM DTT, 1% Triton X-100, 10% glycerol, and 1× protease inhibitor cocktail. After 20 min incubation on ice, the cell lysates were centrifuged at 12 000 rpm for 15 min at 4°C, and the supernatants were recovered. Where indicated, the cell lysates were pre-treated with benzonase nuclease (250 units) for 30 min at room temperature before immunoprecipitation. Indicated antibody (1 μg) was co-incubated with 500 μg cell lysates and 20 μl Protein A/G agarose (Thermo Fisher Scientific) for 12 h at 4°C. The pre-immune IgG (1 μg) was used as control. The precipitates were washed four times with lysis buffer, once with PBS and eluted in 2× loading buffer. Protein samples were resolved by SDS-polyacrylamide gel electrophoresis and blotted onto nitrocellulose membranes, which were blocked in 5% skim milk in PBST and probed with indicated primary antibodies. After being probed with HRP-conjugated anti-mouse, anti-rabbit or Protein A, protein bands were visualized using enhanced chemiluminescence detection system (Thermo Fisher Scientific).

Chromatin immunoprecipitation (ChIP) of telomeric and Alu DNA

Chromatin immunoprecipitation (ChIP) analysis of telomeric and Alu DNA was conducted as previously report method (32,64) with some modifications. Briefly, cells were grown to 80% confluence, then crosslinked with freshly made 1% formaldehyde in PBS for 30 min at 37°C, followed by washing with cold 1 × PBS for three times. Cells were homogenized in lysis buffer (50 mM Tris–HCl pH 8.1, 1% SDS, 5 mM EDTA, 1 mM PMSF and 1× protease inhibitor cocktail) at a density of 1×10^7 cells/ml and incubated for 10 min on ice. The lysates were sonicated on ice and centrifuged for 10 min at 12 000 rpm. Part of supernatant was kept as input, other was 1:5 diluted in dilution buffer (20 mM Tris–HCl pH8.1, 1% Triton X-100, 2 mM EDTA, 150 mM NaCl, 1 mM DTT, 1mM PMSF and 1× protease inhibitor cocktail). Pre-clearing was performed with protein A/G Sepharose beads plus salmon sperm DNA for 2 h at 4°C, followed by immunoprecipitation with indicated antibodies (anti-PRL-3, anti-53BP1, anti-RAD51, 3 μg; anti-shelterin components, 5 μg) and control IgG (5 μg) overnight at 4°C. Precipitates were sequentially washed in TSE buffer I (20 mM Tris–HCl pH 8.1, 0.1% SDS, 1% Triton X-100, 2 mM EDTA, 150 mM NaCl), TSE buffer II (Tris–HCl pH 8.1, 0.1% SDS, 1% Triton X-100, 500 mM NaCl, 1 mM EDTA) and TSE buffer III (10 mM Tris–HCl pH 8.1, 0.25 M LiCl, 1% NP-40, 1% deoxycholate, 1 mM EDTA) for 5 min each time, followed by washing twice with TE buffer. DNA was eluted in freshly prepared buffer containing 1% SDS and 0.1 M $NaHCO_3$, and incubated at 65°C for 16 h to reverse the formaldehyde crosslinking. After boiling for 10 min, 50% (for detection of telomeric DNA) or 20% (for detection of Alu) of precipitated DNA and input DNA were dot-blotted onto nitrocellulose membrane using Bio-Rad BIO-DOT apparatus. DNA was crosslinked to the membrane immediately by UV (200 J/m^2) for 90 s with the Stratalinker 1800, then rinsed in 2× Saline Sodium citrate (SSC) for 5 min. Telomere-specific signals were detected with the Telo-TTAGGG (Roche) kit as per manufacturer's protocols. Alternatively, Alu-specific signals were detected with a biotin-conjugated DNA probe to the 3′-end of the Alu repeat element (5′-CGGGAAGCAGAGGTTGTAGTGAGCC-3′, synthesized by SBS Genetech).

Cytogenetic analysis and fluorescence *in situ* hybridization (FISH) staining

Cells were arrested in 0.1 μg/ml colcemid at 37°C for 1 h, trypsinized, and pelleted at 1000 rpm for 5 min. After incubation in 75 mM KCl at 37°C for 60 min, cells were centrifuged and washed with PBS, then fixed in methanol/acetic acid (3:1) at room temperature for 1 h. Fixed cells were dropped onto slides and air-dried overnight in a chemical hood. The metaphase spreads were subjected to standard chromosome banding analysis after staining the slides with Giemsa stain (2%, v/v).

Fluorescence *in situ* hybridization (FISH) staining of telomeres (Telo-FISH) was performed following previously reported procedures (65) with some modifications. Briefly, slides of metaphase spreads were heated at 65°C in a humidified block for 3 h, followed by fixation in freshly prepared 4% paraformaldehyde at room temperature for 10 min. After being washed with PBS for three times, slides were treated with 100 μg/ml RNase A in 2× SSC at 37°C

for 1 h, washed with 2× SSC for three times and distilled water for one time. The fixation and washing steps were repeated once, and the slides were dehydrated in cold ethanol series (70, 80 and 90%, each for 1 min) and dried on air at room temperature. Slides were heated at 85°C for 10 min, stained with 50 nM pre-heated (65°C) Cy3-PNA probe (Panagene, Daejeon, Korea) in hybridization buffer (20 mM Na_2HPO_4 pH7.4, 20 mM Tris–HCl pH 7.4, 60% formamide, 2× SSC, 0.1 μg/ml salmon sperm DNA) at 85°C for 10 min, then at room temperature for 16 h. Next day, slides were washed with washing buffer I (10 mM Tris–HCl pH 7.2, 70% formamide, 0.1% BSA) for two times, washing buffer II (10 mM Tris–HCl pH 7.2, 1.5 M NaCl, 0.1% Tween 20) for three times, counterstained with 4′,6-Diamidino-2-phenylindole (DAPI) in 2× SSC and mounted with 50% glycerol.

Chromosome orientation FISH (CO-FISH) staining was performed following established procedures (66) with some modifications. Cells were pre-treated with BrdU: BrdC (7.5 μM: 2.5 μM) for 14 h before preparation of metaphase spreads. Slides were treated with RNase A (0.1 mg/ml) in 2× SSC for 60 min at 37°C, followed by exposure to 365-nm ultraviolet (UV) light (Stratalinker 1800) for 30 min. The BrdU/BrdC-substituted DNA was digested with 10 U/μl Exonuclease III (Promega) in 50 mM Tris–HCl pH 8.0, 5 mM $MgCl_2$ and 5 mM DTT for 10 min at room temperature. Chromosomes were briefly denatured in 70% formamide, 2× SSC at 70°C (1 min) and then dehydrated through a cold ethanol series (70, 85 and 100%). Next, slides were stained with 50 nM Cy3-leading strand probe and 50 nM FITC-lagging strand probe (both from Panagene). Chromosomes were counterstained with DAPI.

Immunofluorescence (IF) staining and IF-FISH

Cells were grown on coverslips to 60% confluence. Unless specified, cells were pre-extracted with solution E (0.5% Triton X-100, 3 mM $MgCl_2$, 20 mM Hepes-KOH pH7.9, 50 mM NaCl, 300 mM sucrose) for 30 s, fixed with cold methanol-acetic acid (1:1) for 10 min at 4°C, re-extracted with solution E at room temperature for 10 min and washed with PBS. Alternatively, cells were fixed in freshly prepared 2% paraformaldehyde for 30 min, followed by extraction in 0.5% Triton X-100 in PBS for 5 min. For immunostaining of BrdU, cells were pre-incubated with 10 μM BrdU for 45 min, fixed in 2% paraformaldehyde for 5 min, washed with PBS, denatured in HCl (1.5 M) at 37°C for 30 min and washed with Borate buffer (pH 8.5) for five times. After these steps, cells were blocked with 5% (v/v) goat serum at room temperature for 1 h, and incubated with indicated primary antibodies at room temperature for 1.5 h or at 4°C for 16 h. After washing with 0.1% Tween 20 in PBS for five times, cells were incubated with TRITC- or FITC-conjugated secondary antibodies at room temperature for 45 min, followed by washing with 0.1% Tween 20 in PBS, and counterstaining with DAPI.

For immunofluorescence (IF)-FISH staining, cells were subjected to immunofluorescence staining as per the aforementioned procedures. After being probed with the secondary antibody and washed with 0.1% Tween 20 in PBS, coverslips were fixed again with methanol/acetic acid (1:1) for 10 min at 4°C. Next, coverslips were washed with PBS for three times, treated with 100 μg/ml RNase A in 2× SSC at 37°C for 60 min, washed with 2× SSC for three times and distilled water for one time. The fixation and washing steps were repeated once, then the coverslips were dehydrated in cold ethanol series (70, 80, 90%, each for 1 min), and dried on air at room temperature. Coverslips were heated at 80°C for 10 min, stained with pre-heated 50 nM Cy3-PNA probe in hybridization buffer (20 mM Na_2HPO_4 pH7.4, 20 mM Tris–HCl pH 7.4, 60% formamide, 2× SSC, 0.1 μg/ml salmon sperm DNA) at 85°C for 10 min, then at room temperature for at least 16 h. Subsequently, coverslips were washed twice in 0.1% Tween 20/2× SSC at 65°C for 10 min. After being counterstained with DAPI in 2× SSC for 10 min, the coverslips were sequentially washed with 2× SSC for 2 min, 1× SSC for 2 min, distilled water for 2 min and mounted with 50% Glycerol.

In situ proximity ligation assay (PLA)

HCT116 cells grown on coverslips were pre-extracted in solution E for 20 s, fixed with cold methanol/acetic acid (1:1) for 20 min at 4°C, re-extracted with solution E at room temperature for 10 min, washed with PBS twice and blocked for 30 min with goat serum (5%) in PBS. Next, proximity ligation assay (PLA) staining was performed following the provider's instructions with the Duolink *In Situ* PLA probes (anti-Mouse Minus and anti-Rabbit Plus) and the Duolink In Situ Detection Reagents Red (Olink Bioscience).

Telomere length analysis

Southern blot analysis of telomere length was performed as described previously (67). Genomic DNA (5 μg per sample) from cultured cells or mouse tissues was digested with Hinf I/Rsa I (Promega) and electrophoresed through 0.8% agarose gels in 0.5× TBE using a CHEF MAPPER XA pulsed-field electrophoresis apparatus (Bio-Rad). Separation was continued for 16 h at 5 V/cm at 14°C. After being blotted to the nitrocellulose membrane, DNA fragments were analyzed with a Telo-TTAGGG kit from Roche. Alternatively, telomere length was measured by quantitative PCR (qPCR) method (68,69). Equal amount of genomic DNA (30 ng) was used for each reaction and PCR was performed on the StepOne system (Applied Biosystem). Telomeric primers and primers for the reference control gene were synthesized by GenePharma. For each PCR amplification, a standard curve was generated by serial dilutions of known amounts of DNA. The telomere signal was normalized to the signal from the single copy gene to generate T/S ratio to represent relative telomere length.

Evaluation of mitotic disturbances in human colorectal tissue samples and immunohistochemical staining

The clinicopathological parameters of 273 colorectal cancer patients and the significance of positive PRL-3 expression in prognosis had been reported previously (70). Sections from 273 colorectal cancer tissues, which had been stained with anti-PRL-3 antibody and counterstained with haematoxylin/eosin (HE), were re-examined. Semiquantitative scoring was performed. At × 400 magnification, cells

were analyzed from five areas with maximum tumor staining in each section and the average percentage of positive cells was recorded. The averaged values were stratified into five group: –, no expression;+/–, <10% positive cells; +, 10–20% weakly to moderately stained cells; ++, 10–20% strongly stained cells of 20–50% weakly stained cells; +++, 20–50% positive cells with moderate to strong staining or >50% positive cells. In the statistical analysis, – and +/– were considered as Negative, +, ++, and +++ were considered as Positive. With these grouping criteria, we evaluated correlation between PRL-3 status and mitotic defects in 269 stained section (four sections were excluded because of limited field of view). Microscopic analysis was done by two of the authors (LQ and CL) without knowledge of clinical data and final histopathologic classification. Tissue-chips were obtained from Alenabio (Th802a, thyroid). Immunohistochemical staining of tissue-chips and mouse tissues were carried out following previously reported procedures (70).

Reactive oxygen species (ROS) measurement, β-galactosidase activity, TdT-mediated dUTP nick end labeling (TUNEL) and cell migration assay

Intracellular reactive oxygen species (ROS) levels were determined by staining live cells with the dihydroethidium (DHE) probe from GENMED (Shanghai, China). Cells grown on plates were rinsed with pre-warmed PBS twice and replenished with fresh complete media. Next, cells were stained with DHE (10 μM) for 30 min at 37°C. For control, cells were treated with DMSO (vehicle, 1:1000). Senescence-associated β-galactosidase activity was determined with a kit from GENMED following the manufacturer's instructions. TdT-mediated dUTP nick end labeling (TUNEL) staining of mouse tissues was performed with a kit from Roche. For migration assay, 6.5-mm Transwell chamber with 8.0-μm pore membranes (Corning) was used. The bottom chamber was filled with 800 μl medium containing 10% Fetal Bovine Serum as the chemoattractant. Cells resuspended in serum-free medium were carefully transferred onto the top chamber of each Transwell apparatus at a density of 3×10^5 cells/ml (100 μl per chamber). Cells were allowed to migrate for 20–24 h at 37°C. After that, the top surface of each membrane was cleared of cells with a cotton swab. Cells that had penetrated to the bottom side of the membrane were fixed in methanol, stained with hematoxylin, and counted in nine randomly selected microscopic fields per membrane.

Transgenic mice and dextran sodium sulfate (DSS) model

Animal experiments were approved by the Biomedical Ethical Committee of Peking University Cancer Hospital & Institute and performed along institutional animal welfare protocols concordant with the NIH guidelines. Construction of pTet-on-pTRE2-Ptp4a3 expression construct and microinjection were performed by the Model Animal Research Center, Nanjing Biomedical Research Institute (Nanjing, China). Six generations of mice on C57BL/6J background (>1100 littermates) were screened by PCR of tail DNA to confirm the establishment of *PRL3*-TG mice. Mice were housed in animal facility (with SPF condition) at the Peking University Cancer Hospital & Institute. To induce PRL-3 expression, 8-week-old mice were feed with drinking water containing 1.5 mg/ml of DOX. For DSS model, mice were firstly subjected to 8-week of DOX treatment, followed by 4 cycles of 1-week of 2% DSS without DOX in the drinking water plus 2-week of normal drinking water with DOX. At the end of experiments, mice were sacrificed by euthanasia and colons were opened longitudinally and washed extensively in cold PBS. Tissues were either paraffin embedded for immunohistochemical analysis or FISH staining, snapped frozen for RNA analysis or homogenized in RIPA buffer for protein analysis.

Quantative RT-PCR (qRT-PCR) and tissue-scan cDNA assay

Tissue-Scan human colon cancer and normal tissue cDNA arrays (HCRT305) were obtained from OriGene. For mouse colon tissues, total RNA was extract with Trizol Reagent (Invitrogen). qRT-PCR reactions were performed with StepOne system using SYBR Green according to manufacturer's instructions. Program for amplification was: 95°C for 30 s, followed by 40 cycles of 95°C for 30 s, 60°C for 30 s and 72°C for 30 s. The following sense and antisense primers were were synthesized by GenePharma: human *PRL3*, 5′-GGGACTTCTCAGGTCGTGTC-3′, 5′-AGCCCCGTACTTCTTCAGGT-3′; human *RAP1*, 5′-CACCCGGGAGTTTGA-3′, 5′-GTGGATCATCATCACACATAGT-3′; human *TERF2*, 5′-GGTACGGGGACTTCAGACAG-3′, 5′-CGCGACAGACACTGCATAAC-3′; human *GDPDH*, 5′-CATCAAGAAGGTGGTGAAGCAG-3′, 5′-CGTCAAAGGTGGAGGAGTGG-3′; mouse *PRL3*, 5′-GTGGTAGAGGACTGGCTGAG-3′, 5′-TTCTGTCGGATGAACTGGAT-3′; mouse *CCND1*, 5′-CTGCAAATGGAACTGCTTCTGGTGA-3′, 5′- AGCAGGAGAGGAAGTTGTTGGGGCT-3′; mouse *IL1A*, 5′-GAGAGCCGGGTGACAGTATC-3′, 5′- TGACAAACTTCTGCCTGACG-3′; mouse *IL6*, 5′-AGTTGCCTTCTTGGGACTGA-3′, 5′- CAGAATTGCCATTGCACAAC-3′; mouse *TGFB*, 5′-GGAGGTACCGCCCGGCCCGC-3′, 5′-GACAGCAATGGGGGTTCGGG-3′; mouse *COX2*, 5′-AAAAGCTGGGAAGCCTTCTC-3′, 5′-AAGTGCTGGGCAAAGAATGC-3′; mouse *TNFA*, 5′-CGTCAGCCGATTTGCTATCT-3′, 5′-CGGACTCCGCAAAGTCTAAG-3′; mouse *OCLN*, 5′-TTGAAAGTCCACCTCCTTACAGA-3′, 5′-CCGGATAAAAAGAGTACGCTGG-3′; mouse *CXCL1*, 5′-ACTGCACCCAAACCGAAGTC-3′, 5′-TGGGGACACCTTTTAGCATCTT-3′; mouse *GAPDH*, 5′-CTTCACCACCATGGAGGAGGC-3′, 5′-GGCATGGACTGTGGTCATGAG-3′. The expression levels for all the genes were normalized to *GAPDH*, and the data were analyzed using the 2-ΔΔCt method.

Image acquisition

X-ray films of western blot, Southern blot, EMSA and ChIP blot were digitized on a Canon CanoScan LiDE100 scanner with linear intensity settings. Fluorescence images of IF,

PLA, FISH, IF-FISH and TUNEL were acquired with the Leica TCS SP5 confocal microscope system (60x oil, NA 1.40 Plan-ApoChromat, including two HyD detectors) at fixed exposure settings at room temperature. Images of CO-FISH were taken with the Zeiss LSM800 confocal system (63× oil, NA 1.40 Plan-ApoChromat, including two gasp detectors) at fixed exposure settings at room temperature. For co-localization studies, multi-channel/track and two-color sequential line scanning were applied to avoid bleach-through, cross talk or movement-dependent signal correlation. DHE staining of live cells were observed with the Leica TCS SP5 confocal microscope system at fixed exposure settings at 37°C. Intensities of telomeres and DHE fluorescence were quantified by LAS-AF software. β-galactosidase staining of cells and immunohistochemical staining of tissue sections were observed under a Nikon Eclipse 80i microscope equipped with Nikon DS-Fi1 camera. Digital images were processed with Adobe Photoshop CS by adjusting the linear image intensity display range. Optical densities (OD) of ChIP blots and western blots were quantified by Scion Image.

Statically analysis

Data analysis was performed using SPSS 12.0. Where indicated, the standard $\chi 2$ test, two-tailed student's *t*-test, or two-way analysis of variance (ANOVA) was used to determine the significance of differences. Values represent mean ± SD. *P* value less than 0.05 was considered statistically significant.

RESULTS

RAP1 mediates PRL-3–TRF2 interaction

Previously we identified shelterin component RAP1 as a PRL-3-associated protein (10). With purified GST-PRL-3, we precipitated both RAP1 and TRF2 from HCT116 cell lysates in a pull-down assay (Figure 1A). In an attempt to investigate functions of endogenous PRL-3 and its physical interaction with shelterin components, we generated a PRL-3-specific monoclonal antibody (clone 4G8), which recognized both recombinant and endogenous PRL-3 and could be employed for western blot and inmunofluorescence staining (Supplementary Figure S1A–D). The specificity of this antibody was further characterized by diminished signals after transient transfection of PRL-3-specific siRNAs (Supplementary Figure S1B and C). Using this antibody, TRF2 and RAP1 were immunoprecipitated from HCT116 cell lysates (Figure 1B, upper panel). Reciprocal immunoprecipitation with an antibody to RAP1 confirmed the existence of a ternary complex containing PRL-3, RAP1, and TRF2 (Figure 1B, lower panel). By using purified recombinant proteins (Supplementary Figure S1E), we performed in vitro binding assay. In contrast to the direct binding between RAP1 and PRL-3 (10), GST-TRF2 failed to precipitate His-PRL-3, but the interaction between them was detected after co-incubation with His-RAP1 (Figure 1C). TRF2 and RAP1 can associate with both telomeric and extra-telomeric DNA repeats (48,71), and TRF2 also has RNA-binding activity (72). To rule out the possibility that PRL-3–RAP1–TRF2 complex is bridged by DNA or RNA, cell lysates or mixtures of purified proteins were pretreated with benzonase nuclease. We found that such treatment didn't affect the efficiency of immunoprecipitation or pull-down (Figure 1B and C), suggesting that formation of PRL-3–RAP1–TRF2 complex is independent of DNA or RNA. In addition, result of immunoprecipitation assay showed that more TRF2 was precipitated by anti-PRL-3 in COS7 cells overexpressing RAP1 (Figure 1D). Conversely, less TRF2 was recovered in the anti-PRL-3 immunoprecipitates after transient knockdown of RAP1 in HCT116 cells (Figure 1E). The adaptor role of RAP1 in mediating both protein–protein and protein–DNA interactions has been demonstrated previously (35). Our present study underlined this function in a distinct context. To delineate the sequence basis of the RAP1 adaptor function, we purified a panel of GST-tagged deletion mutants of RAP1 for the in vitro binding assay (Supplementary Figure S1E). The Myb domain was characterized as the region essential for RAP1's interaction with PRL-3 (Figure 1F). Consistent with this result and previous studies showing that RCT domain of RAP1 is required for its association with TRF2 (40), mutant RAP1 lacking either Myb or RCT domain failed to mediate TRF2–PRL-3 interaction in the pull-down assay (Figure 1G). Expression of GFP-Myb in HCT116 cells had no effect on RAP1–TRF2 interaction, but abolished RAP1-PRL-3 interaction in immunoprecipitation assay (Figure 1H), emphasizing the contribution of the Myb domain to maintain PRL-3–RAP1–TRF2 complex in cells. Myb domain of RAP1 was also partially required for its association with Ku80 (73). We found GFP-Myb had no obvious effect on Ku80-RAP1 interaction (Figure 1H).

RAP1 and TRF2-dependent recruitment of PRL-3 to telomeric DNA

The nuclear localization of PRL-3 has been reported previously (19,74). We observed nuclear PRL-3 by immunofluorescence staining (Supplementary Figure S1C), which was more evident in cells briefly extracted before fixation (Supplementary Figure S2A). Through subcellular fractionation, PRL-3 was detected in cytoplasma, nucleoplasma, and chromatin-enriched fractions (Supplementary Figure S2B). After release from double thymidine block, cell cycle-dependent changes of PRL-3 in distinct fractions were revealed (Supplementary Figure S2B). Notably, PRL-3 partially colocalized with both RAP1 and TRF2 (Supplementary Figure S2A), which is consistent with the existence of PRL-3-RAP1-TRF2 complex. To exclude the possibility that these observed co-localizations were merely random overlapping, we performed *in situ* PLA staining, through which both PRL-3-RAP1 and PRL-3-TRF2 interactions were revealed (Figure 2A). Because of specific binding of TRF2–RAP1 complex to telomeres (31,32), we evaluated PRL-3′s physical presence on telomeres. By using purified myc-TRF2, His-RAP1, and His-PRL-3 (Supplementary Figure S1E), we found that His-PRL-3 alone could not be precipitated by synthesized telomeric DNA or Alu DNA in the in vitro binding assay, while co-incubation with His-RAP1 and myc-TRF2 enabled recruitment of PRL-3 to telomeric DNA (Figure 2B). IF-FISH staining with anti-PRL-3 mAb (4G8) and probe for telomere showed that a

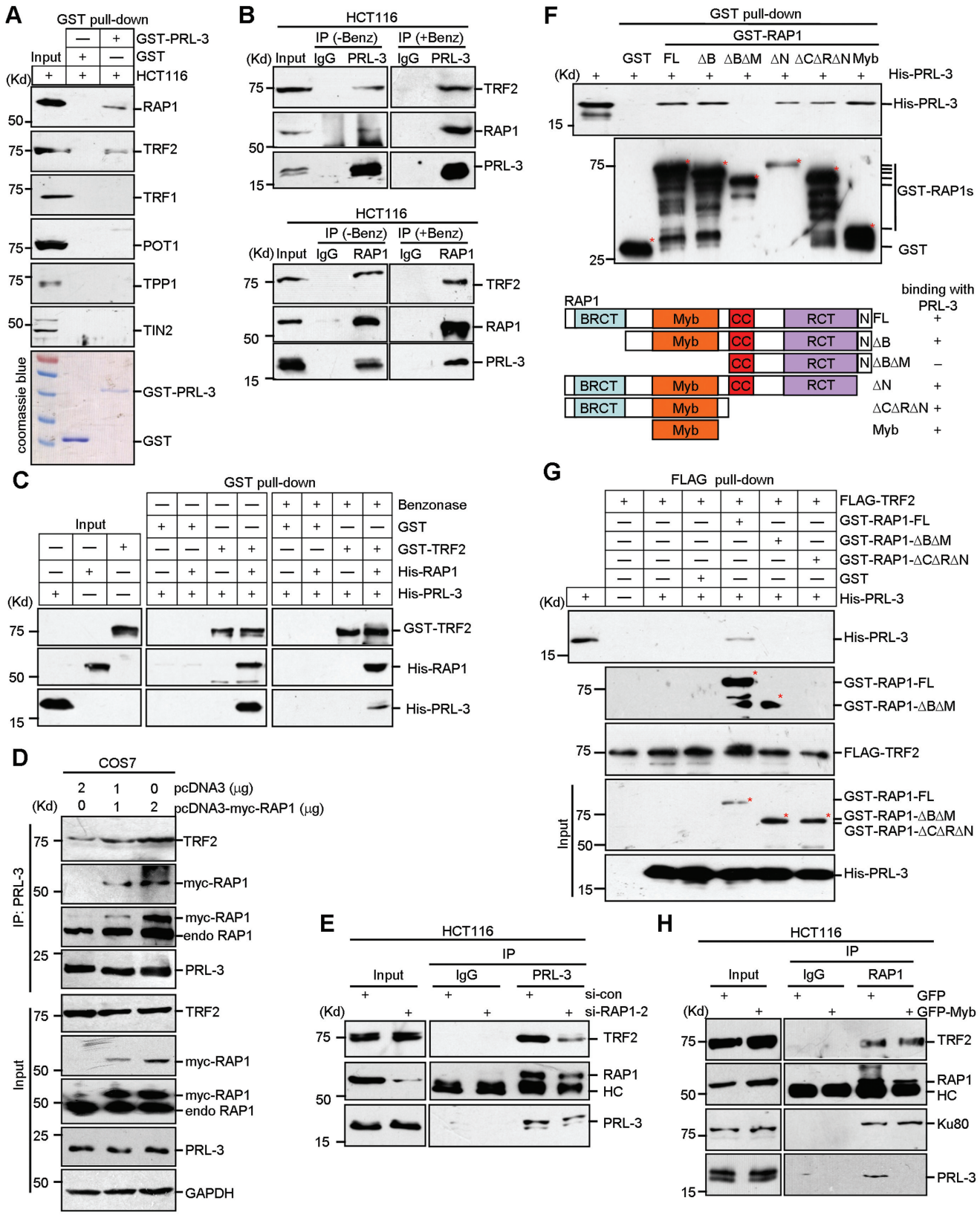

Figure 1. RAP1 mediates PRL-3–TRF2 interaction. (**A**) Precipitation of endogenous RAP1 and TRF2 by GST-PRL-3. HCT116 cell lysates (500 μg) were co-incubated with 1 μg purified GST (lane 2) or GST-PRL-3 (lane 3), and subjected to GST pull-down with Glutathione-agarose beads. Precipitates and 50 μg HCT116 cell lysates (lane 1, input) were analyzed by western blot with indicated anti-shelterin antibodies. Purities of GST-PRL-3 and GST were verified by Coomassie blue staining (lower panel). (**B**) Endogenous PRL-3 associates with RAP1 and TRF2 in cells in a DNA/RNA-independent

small subset of nuclear PRL-3 co-localized with telomeric DNA in HCT116 cells (Figure 2C and D). Transient knockdown of RAP1 or TRF2 did not affect the protein levels of PRL-3 (Figure 2E), but nuclear abundance and telomere localization of PRL-3 were decreased (Figure 2C and D). To rule out the possibility that observed co-localizations with telomeres were random overlapping, we performed ChIP analysis of telomeric DNA with anti-PRL-3 mAb (4G8), which confirmed the specific association of PRL-3 with telomeric DNA and the requirement of RAP1 and TRF2 (Figure 2F).

Silencing of PRL-3 promotes DDR and senescence, but does not induce telomere deprotection

In light of the telomere localization of PRL-3, we examined effect of PRL-3 on telomere integrity. Because PRL-3 protein was undetected in primary human fibroblasts WI38 or IMR90 (Supplementary Figure S1D), we used human colon cancer cells expressing endogenous PRL-3. Stable knockdown of PRL-3 in HCT116 cells was achieved by lentivirus-mediated transduction of two shRNAs targeting PRL-3 (Figure 3A, left panel). For SW480 cells, CRISPR/Cas9 system was used to knock out PRL-3 (Figure 3A, right panel). Immunofluorescence staining showed that phosphorylated ATM at Ser1981 was activated by PRL-3 silencing (Supplementary Figure S3A), suggesting enhanced DNA damage response. Increased phospho-H2AX (γH2AX) was also detected (Figure 3B). However, phosphorylated CHK1 at Ser345 was unaffected (Figure 3B). IF-FISH staining of γH2AX and telomeric DNA in HCT116 cells revealed no significant changes in Telomere Dysfunction-Induced Foci (TIF) (Figure 3C). In addition, quantitative PCR (qPCR) analysis showed that PRL-3 silencing did not affect telomere length (Supplementary Figure S3B), which was verified by Southern blot analysis of telomere restriction fragment (Supplementary Figure S3C). Anaphase bridges (APB) may give rise to structural and numerical alterations of chromosomes and are closely related to chromosomal instability and tumorigenesis (55). Several conditions could increase anaphase bridge formation, including mutations in telomeric DNA (75), removal of shelterin components (76), telomere shortening (55) and telomere crisis induced by replication inhibitors, such as aphidicolin (77). Micronuclei (MN), generated by lagging chromosomes, also represents a form of chromosomal mis-segregation (78). Silencing of PRL-3 did not change the incidence of anaphase bridge or micronuclei, even in the presence of aphidicolin (Figure 3D), implying that deficiency of PRL-3 has no obvious effects on the telomere integrity or chromosomal stability in HCT116 and SW480 cells. By ChIP analysis of telomeric DNA, we noticed that silencing of PRL-3 decreased telomere association of RAP1 (Figure 3E), possibly because of lowered expression of RAP1 (Figure 3A). We previously found that PRL-3 could promote RAP1 transcription (10). Consistently, qRT-PCR analysis of a colon cancer cDNA array confirmed the positive correlation between transcripts of PRL-3 and RAP1 (Supplementary Figure S3D). No effect of PRL-3 silencing on TRF2 expression or its telomere localization was observed (Figure 3A and E), and there is no correlation between PRL-3 and TRF2 transcripts (Supplementary Figure S3D). Protein levels of Ku70, a cofactor essential for securing telomeric DNA through its cooperation with TRF2 and RAP1 (32), remained relatively stable after PRL-3 silencing (Figure 3A).

After PRL-3 silencing, cell proliferation decreased, as monitored by cell number counting (Supplementary Figure S3E). β-galactosidase staining revealed higher percentages of stained cells after PRL-3 silencing (Figure 3F and Supplementary Figure S3F), indicating that cellular senescence was induced. Interestingly, PRL-3 silencing increased ROS status, as shown by DHE staining (Supplementary Figure S3G). Treatment with ROS chelator N-Acetyl-l-cysteine (NAC) or glutathione (GSH) attenuated both senescence (Figure 3F and Supplementary Figure S3F) and γH2AX levels (Figure 3F) resulted from PRL-3 silencing. These results unveil that PRL-3 deficiency has no effects on telomere integrity or chromosomal stability, but could induce senescence and DDR in a ROS-dependent fashion.

Overexpression of PRL-3 promotes telomere dysfunction

Next, we evaluated the effects of PRL-3 gain-of-function. Exogenous PRL-3 with myc-tag was stably overexpressed in HCT116 and LoVo cells, and its level was higher than

←

manner. HCT116 cell lysates (500 μg) were immunoprecipitated by 1 μg antibody against PRL-3 (upper panel) or RAP1 (lower panel). For control, 1 μg preimmune IgG was used. Parts of lysates were also pre-treated with benzonase (Benz) for 30 min at room temperature before immunoprecipitation. Precipitates and 25 μg HCT116 cell lysates (input) were subjected to western blot. (**C**) Requirement of RAP1 for PRL-3-TRF2 association *in vitro*. Purified proteins (100 ng each) were mixed as indicated (lanes 4–11) and subjected to GST pull-down assay. Some of mixtures were also pre-treated with benzonase for 30 min at room temperature (lanes 8–11). Precipitates and purified proteins (10 ng each, lanes 1–3, input) were analyzed by western blot with antibodies to TRF2, RAP1 and PRL-3. (**D**) Enhancement of PRL-3–TRF2 interaction by RAP1 in cells. COS7 cells were co-transfected with indicated amounts of pcDNA3 and pcDNA3-myc-RAP1 plasmids. The total amount of plasmids for each sample was adjusted to 2 μg. After 48 h, cells were harvested and lysates were immunoprecipitated with anti-PRL-3 and analyzed by western blot with antibodies to TRF2, myc-tag, RAP1 and PRL-3. (**E**) Requirement of RAP1 for PRL-3–TRF2 association in cells. HCT116 cells were transfected with 50 nM control or RAP1-specific siRNA for 48 h. Cell lysates were immunoprecipitated with anti-PRL-3. HC, IgG heavy chain. (**F**) Upper, GST pull-down assay to map the domain of RAP1 required for its interaction with PRL-3. A total of 100 ng GST (lane 2) or GST-RAP1s (lanes 3–8) was co-incubated with 100 ng His-PRL-3 (lanes 2–8). After pull-down, precipitates were detected by anti-PRL3 and anti-GST. Input, 10 ng His-PRL-3 (lane 1). Lower, summary of binding. FL, full-length RAP1; ΔB, deletion of BRCT domain; ΔBΔM, deletion of BRCT and Myb domains; ΔCΔRΔN, deletion of coiled-coil, RCT and NLS domains. Red asterisks, position of GST or GST fusion proteins. (**G**) Adaptor function of RAP1 in mediating TRF2 and PRL-3 interaction is dependent on its Myb and RCT domains. Purified FALG-TRF2, GST-RAP1 (FL, ΔBΔM, ΔCΔRΔN) and His-PRL-3 proteins (100 ng each) were mixed as indicated. Five percent of mixtures were kept as input, and the rests were subjected to pull-down with anti-FLAG-agarose bead. Precipitates and input were analyzed by western blot with antibodies to PRL-3, TRF2 and GST-tag. (**H**) Blockade of PRL-3's recruitment to RAP1–TRF2 complex by GFP-Myb. HCT116 cells were transfected with 0.5 μg of pEGFP-N1 or pEGFP-N1-Myb plasmid for 48 h. Lysates (500 μg) were immunoprecipitated with 1 μg anti-RAP1 or pre-immune IgG. Precipitates and 25 μg lysates (input) were analyzed by western blot.

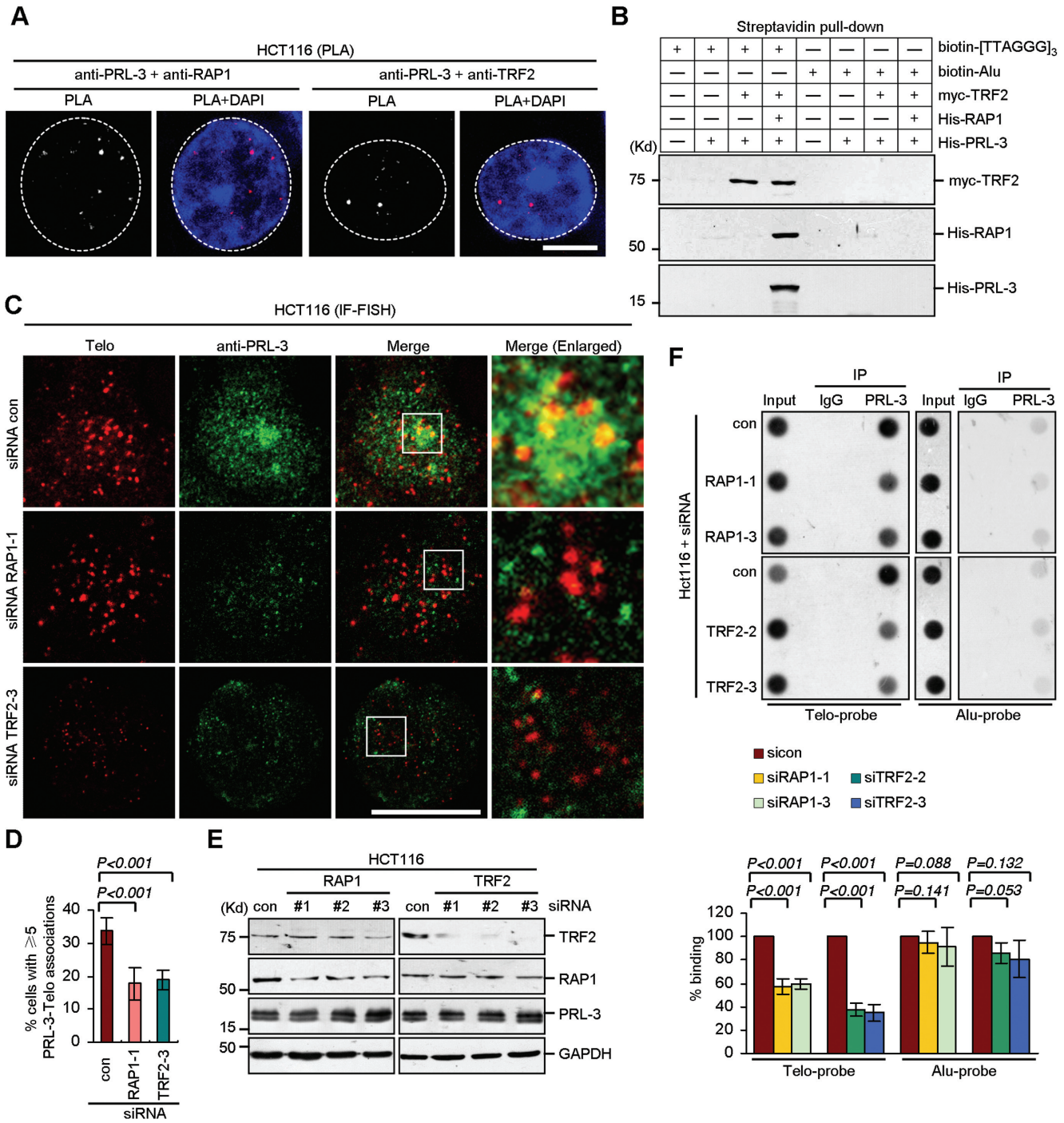

Figure 2. RAP1 and TRF2-dependent recruitment of PRL-3 to telomere. (**A**) *In situ* PLA analysis of PRL-3's associations with RAP1 and TRF2. HCT116 cells were pre-extracted, fixed, inmunostained with indicated pairs of antibodies and probed with Duolink *in situ* PLA reagent. Binding foci were in red and dashed lines indicated outline of nucleus (determined by DAPI counter staining). Scale bar, 10 μm. (**B**) TRF2- and RAP1-dependent recruitment of PRL-3 to telomeric DNA *in vitro*. Purified myc-TRF2 (150 ng), His-RAP1 (120 ng), and His-PRL-3 (30 ng) were co-incubated with 1 μg biotin-labeled telomere (lanes 1–4) or Alu (lanes 5–8) probe as indicated and subjected to pull-down analysis with Streptavidin agarose. Precipitates were analyzed by western blot with antibodies to TRF2, RAP1 and PRL-3. (**C** and **D**) TRF2 and RAP1-dependent recruitment of PRL-3 to telomere in cells. HCT116 cells were transfected with 50 nM indicated siRNAs for 48 h, pre-extracted, fixed and subjected to IF-FISH staining. (C) Representative PRL-3 association with telomere. Scale bar, 10 μm. Areas in white squares were enlarged. (D) Quantification of cells with ≥5 associations between PRL-3 foci and telomere. Mean ± SD of three independent experiments. $n > 100$ cells per single experiment. Student's *t*-test. (**E**) Knockdown efficiencies of RAP1 and TRF2. HCT116 cells were transfected with 50 nM siRNAs against RAP1 or TRF2 for 48 h. Lysates were analyzed by western blot with indicated antibodies. (**F**) ChIP analysis of PRL-3 binding to telomeric and Alu DNA. HCT116 cells were transfected with 50 nM indicated siRNAs for 48 h and processed for ChIP using anti-PRL-3 or pre-immune IgG. Upper, representative blots of hybridization with probe to telomere or Alu. Input, 2% DNA. Lower, quantification of relative optical densities (OD). Relative OD was calculated by normalizing to OD of Input and relative OD of control siRNA-transfected sample was set as 100%. Mean ± SD of three independent experiments. Student's *t*-test.

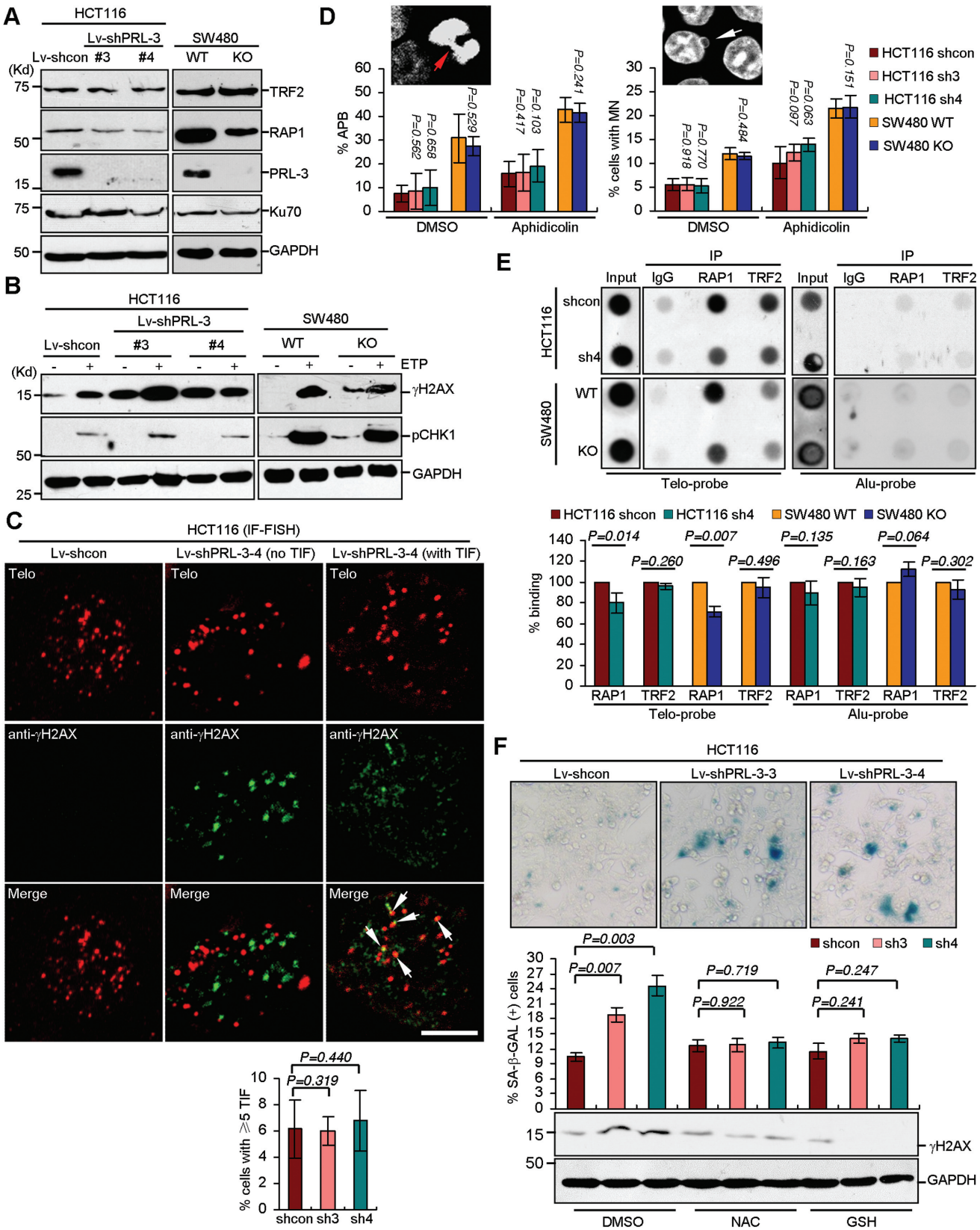

Figure 3. Silencing of PRL-3 promotes DDR and senescence. (**A**) Efficiencies of PRL-3 silencing in HCT116 (knockdown by two shRNAs using lentivirus system, left) and SW480 (knockout by CRISPR/Cas9 system, right) cells and its effects on indicated protein levels. WT, wild-type. KO, knockout. (**B**) Ef-

the endogenous PRL-3 (Figure 4A). Through subcellular fractionation, we found that myc-PRL-3 exhibited similar profile of distribution in cytoplasmic, nucleoplasmic and chromatin-enriched fractions as that of endogenous PRL-3 (Supplementary Figure S4A). Partial co-localization between myc-PRL-3 and endogenous RAP1 was also observed (Supplementary Figure S4B). Additionally, association of myc-PRL-3 to telomeric DNA was detected by ChIP analysis (Supplementary Figure S4C). Thus, myc-tag did not affect the PRL-3 subcellular localization, its association with RAP1 or its binding to telomeric DNA. To further exclude the potential interference of tag, we stably overexpressed untagged PRL-3 in WI38 fibroblasts (Figure 4A). Western blot analysis detected increased phosphorylations of H2AX and CHK1 in HCT116 and WI38 cells overexpressing PRL-3 (Figure 4B). Moreover, increased phosphorylations of H2AX, ATM and CHK2 were revealed by immunostaining (Supplementary Figure S4D), therefore PRL-3 overexpression could induce DNA damage response. Contrary to ROS induction by PRL-3 silencing (Supplementary Figure S3G), DHE staining showed no changes in ROS status upon PRL-3 overexpression (Supplementary Figure S4E). TIF analysis by IF-FISH staining found that telomeric DNA had elevated co-localization with pATM in WI38 cells (Figure 4C) or with γH2AX in HCT116 cells (Supplementary Figure S4F), suggesting that telomeric DNA was damaged and telomere dysfunction was induced by PRL-3 overexpression. Through FISH staining of the metaphase HCT116 cells, we observed that there was prominent loss of telomeric DNA by overexpressing PRL-3 (Supplementary Figure S4G). The higher incidence of telomere fusion, including both chromosome-type fusion and sister chromatid-type fusion (Supplementary Figure S4G), implied an accelerated NHEJ-dependent telomere repair by PRL-3 overexpression. Multiple telomere signals (MTS), one of indicators of telomere fragility and aberrant telomere replication (48), was also increased by PRL-3 overexpression (Supplementary Figure S4G). To further examine PRL-3-induced telomere dysfunction, we performed CO-FISH staining with WI38 cells. We confirmed high levels of telomere fusion induced by PRL-3 overexpression (Figure 4D). Furthermore, we found PRL-3 overexpression promoted telomere sister chromatid exchanges (T-SCEs) and loss of telomeric DNA in both lagging and leading strands (Figure 4D). These results suggest that PRL-3 has a capacity to deregulate telomere replication and stimulate HDR- and NHEJ-dependent telomere repair pathways. Consistent with loss of telomeric DNA (Figure 4D and Supplementary Figure S4G), telomere restriction fragment assay showed that both the length and intensity of telomeric DNA were decreased by PRL-3 overexpression in WI38 and HCT116 cells (Figure 4E), which was corroborated by qPCR analysis of telomere length (Figure 4F).

Overexpression of PRL-3 promotes chromosomal instability and senescence

Above results suggest that PRL-3 overexpression could promote telomere deprotection. Telomere deprotection is associated with chromosomal mis-segregation through enhanced breakage-fusion-bridge events (79,80). Because of the adverse effect of PRL-3 overexpression on telomere integrity, we analyzed its impact on chromosomal stability. PRL-3-induced phosphorylations of H2AX, ATM and CHK2 were always associated with more hallmarks of chromosomal mis-segregation (Supplementary Figure S4D). By quantification, more micronuclei and anaphase bridges were observed in HCT116 and WI38 cells overexpressing PRL-3, which were further induced by aphidicolin (Figure 5A). Through cytogenetic analysis, we found that PRL-3 promoted numerical and structural abnormalities of chromosomes (Supplementary Figure S5A). Therefore, PRL-3 overexpression promotes chromosomal instability. PRL-3 overexpression resulted in decreased BrdU incorporation (Figure 5B). Furthermore, we observed an increased β-galactosidase positive rates in PRL-3 overexpressing cells, indicating that PRL-3 overexpression could boost cellular senescence (Figure 5C). These results were supported by immunostaining of heterochromatin marker H3K9me3 (Figure 5D), another indicator of senescence (29,81). In light of PRL-3-promoted DNA damage response (Figure 4B and Supplementary Figure S4D), we treated cells with ATM kinase inhibitor Ku55933 and found that PRL-3-induced β-galactosidase activity was abolished (Figure 5C). Thus, ATM signaling pathway may play a role in mediating PRL-3-provoked senescence. Associated with senescence, cell number counting showed that PRL-3 overexpression decreased cell proliferation (Supplementary Figure S5B), despite of the known ability of PRL-3 to promote cell motility in the transwell chamber migration assay (Supplementary Figure S5C).

In addition to the stable overexpression of myc-tagged or untagged PRL-3, we also transiently overexpressed untagged PRL-3 in HCT116 cells stable knockdown for PRL-3, which was generated by using a shRNA targeting the 3′-

←

fects of PRL-3 silencing on phosphorylations of H2AX and CHK1. Samples treated with 20 μM etoposide (ETP) for 4 h were used as positive controls. (**C**) Effects of PRL-3 silencing on TIF formation. Indicated HCT116 cells were subjected to IF-FISH staining. Upper, representative staining. Arrows, colocalizations between γH2AX and telomere (TIFs). Scale bar, 5 μm. Lower, quantification of cells with ≥5 TIF. Mean ± SD of two independent experiments. $n > 200$ cells per single experiment. Student's *t*-test. (**D**) Effects of PRL-3 silencing on anaphase bridges (APB) and micronuclei (MN) formation. Indicated cells were treated with aphidicolin (0.2 μM) or DMSO (1:1000) for 24 h, followed by DAPI staining. Mean ± SD of two independent experiments. $n > 1000$ cells scored per sample for MN and $n > 50$ anaphase cells scored per sample for APB. Student's *t*-test. Representative images of APB (red arrow) and MN (white arrow) of HCT116 cells stained with DAPI were shown. (**E**) ChIP analysis of RAP1 and TRF2's binding to telomeric or Alu DNA in HCT116 and S480 cells silenced for PRL-3. Upper, representative blots after ChIP with indicated antibodies or IgG. Input, 2% DNA. Lower, quantification of relative OD. Relative OD was calculated by normalizing to that of input and relative OD of control was set as 100%. Mean ± SD of three independent experiments. Student's *t*-test. (**F**) PRL-3 silencing induced ROS-dependent cellular senescence and DNA damage response. Indicated HCT116 cells were treated with NAC (10 mM), GSH (10 mM) or DMSO (1:1000) for 24 h. Part of cells were fixed and processed for β-galactosidase staining, others were analyzed by western blot. Upper, representative β-galactosidase staining of cells treated with DMSO. Middle, quantification of β-galactosidase positive cells. Mean ± SD of two independent experiments. $n > 400$ cells per single experiment. Student's *t*-test. Lower, western blot of γH2AX.

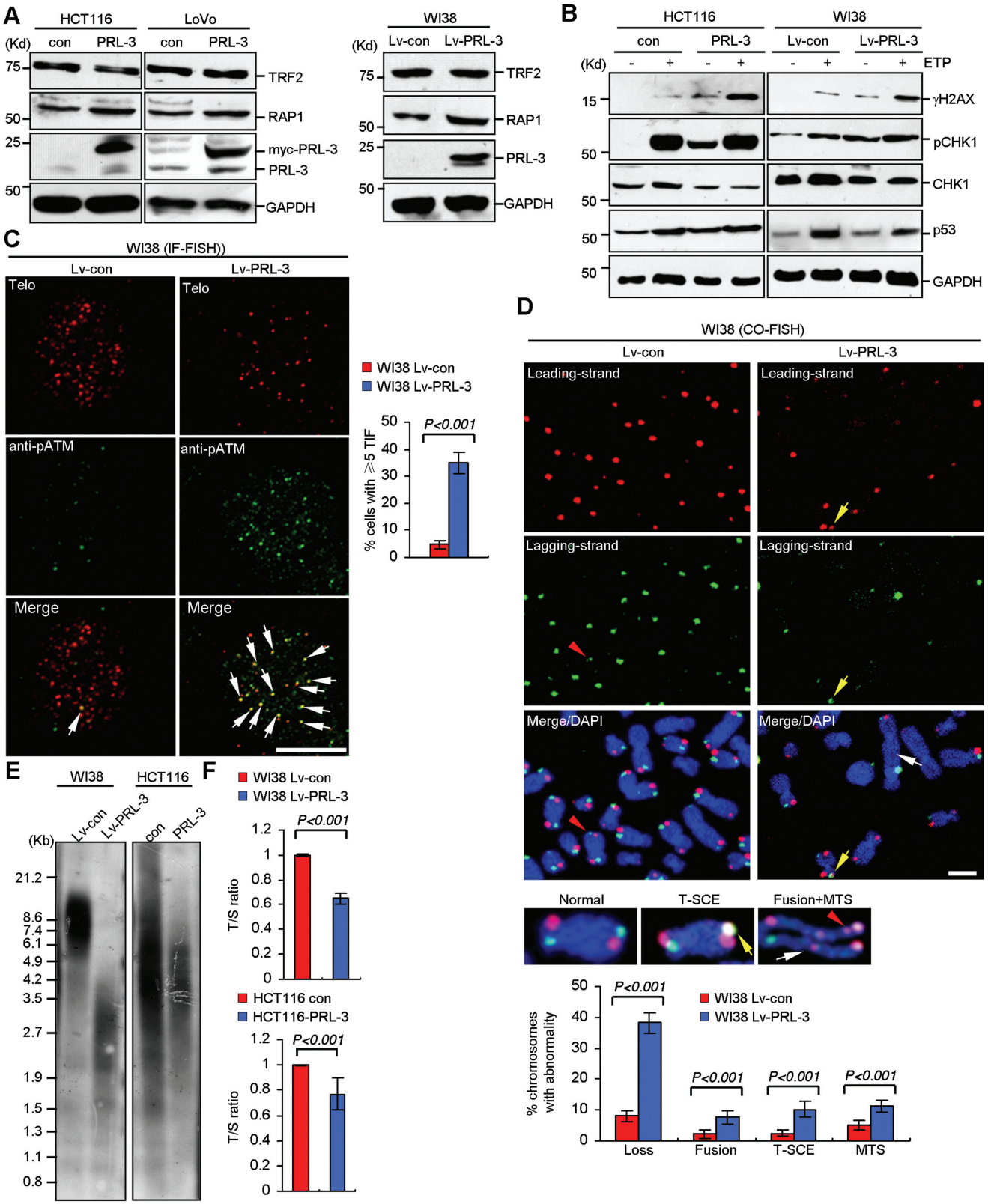

Figure 4. Overexpression of PRL-3 promotes telomere dysfunction. (**A**) Validation of PRL-3 stable overexpression. WI38 fibroblasts were infected with control or PRL-3-expressing letivirus. Expression vectors pcDNA3-myc-PRL-3 (for HCT116 cells), pcDNA3.1-myc-PRL-3 (for LoVo cells) and the respective control plasmids were transfected into cells, followed by selection and pooling of stable colonies. Cell lysates were examined by western blot with antibodies to PRL-3, TRF2 and RAP1. (**B**) Effects of PRL-3 stable overexpression on γH2AX, pCHK1 and p53 levels. Indicated cells were treated with

UTR of PRL-3 mRNA (Figure 5E). Genomic DNA was extracted and subjected to qPCR analysis of telomere length, while cell lysates were used for western blot. After calculation of relative telomere length and quantification of relative protein expression, we found PRL-3 had an inverse correlation with telomere length and positive correlations with γH2AX and H3K9me3 (Figure 5E), further illustrating the ability of PRL-3 to induce telomere deprotection, DNA damage and senescence upon its overexpression in cells.

PRL-3 level positively correlates with telomere deprotection and senescence in clinical samples

To substantiate the results from cultured cells overexpressing PRL-3, we retrospectively analyzed a cohort of colorectal cancer tissues ($n = 269$) stained with anti-PRL-3 (clone 3B6) (70). Although the majority of mitotic cells were bipolar, more multipolar mitoses, an indicator of chromosomal mis-segregation and chromosomal instability (82), was observed in PRL-3 positive tissues than in negative tissues (Figure 6A). Also in the PRL-3 positive tissues, more anaphase bridges were detected (Figure 6A). These results suggest that PRL-3 levels positively correlate with chromosomal instability in colon cancer tissues. Next, we analyzed 12 freshly dissected colon cancer tissues, with WI38 control and PRL-3-overexpressing cells as reference samples (Figure 6B). We detected varying levels of PRL-3 proteins in these tissues, and the level of stably overexpressed PRL-3 in WI38 cells was comparable to some of these tissues. An inverse correlation between PRL-3 and telomere length was revealed, while PRL-3 showed positive correlations with γH2AX and H3K9me3 (Figure 6B). These results suggest that the effects of PRL-3 expression in colon cancer tissues could be mimicked by the stable overexpression system in cultured cells. We also performed quantitative FISH (qFISH) analysis of telomere length and immunohistochemical staining of PRL-3 with thyroid tissue-chips containing 80 samples. We found decreased telomere staining in adenocarcinoma tissues ($n = 40$) with positive PRL-3 expression, particularly in those of Stage I ($n = 23$) (Figure 6C). No correlation was observed in thyroid adenoma ($n = 40$) or Stage II/III/IV adenocarcinoma ($n = 17$) (Figure 6C). With the same thyroid tissue-chip, we evaluated association between PRL-3 and senescence. In Stage I thyroid adenocarcinoma tissues, positive staining of PRL-3 correlated with positive H3K9me3 staining, but such correlation was not observed in thyroid adenoma or Stage II/III/IV adenocarcinoma (Figure 6D). These results raise the possibility that PRL-3-promoted telomere deprotection and senescence are early events during the development and progression of thyroid cancer.

PRL-3 promotes removal of RAP1 and TRF2 from telomeric DNA

Our results revealed that overexpression of PRL-3 promotes telomere deprotection, DNA damage response, chromosomal instability and senescence in both cultured cells and clinical samples. Subsequently, we sought to explore the mechanism(s) underlying these effects. Previously we found overexpression of PRL-3 could increase RAP1 expression and relocate RAP1 from the nucleus to the cytoplasma (10). Unlike RAP1, relocation of other five shelterin proteins to cytoplasma was not observed in HCT116 cells overexpressing PRL-3 (Supplementary Figure S6A). Through differential extraction of chromatin-enriched fractions by using increasing concentrations of NaCl, we found that TRF1 levels were not affected by PRL-3 overexpression; however, TRF2 and RAP1 levels were significantly decreased (Figure 7A). It should be mentioned that PRL-3 overexpression promoted RAP1 expression, but did not change protein levels of TRF2 (Figure 4A). Next we evaluated associations of TRF2 and RAP1 with telomeric DNA in cells. We performed ChIP analysis of telomeric DNA and found that overexpression of PRL-3 decreased telomere-bound TRF2 and RAP1 in both WI38 and HCT116 cells (Figure 7B). We also analyzed telomere bindings of other four shelterin component as well as 53BP1 and RAD51, two proteins appreciated for their pivotal roles in repair pathways of telomere (53). Interestingly, telomere-bound TPP1, POT, TIN2, RAD51 and 53BP1 were increased in HCT116 cells overexpressing PRL-3 (Supplementary Figure S6B). 53BP1 is also served as a canonical marker for DNA breakages (31,83), thus increased telomere loading of 53BP1 in HCT116 cells further supported results of TIF analysis (Supplementary Figure S4F). The removal of TRF2 and RAP1 from telomeric DNA by PRL-3 was substantiated by IF-FISH analysis of WI38 and HCT116 cells overexpressing PRL-3 (Figure 7C and Supplementary Figure S6C). To support the above results, we performed EMSA analysis by using purified proteins (Supplementary Figure S6D) plus synthesized telomeric DNA. Equal moles of TRF2 and RAP1 formed a complex with $[TTAGGG]_{12}$ duplex DNA (complex I, Figure 7D, lane 3). Consistent with the results of *in vitro* binding assay (Figure 2B), purified PRL-3 protein alone failed to bind DNA substrate, while co-incubating PRL-3 with TRF2 and RAP1 induced a faster migrating complex (Complex II, Figure 7D, lane 4). Addition of antibody to PRL-3 or TRF2 induced similar pattern of super-

←

ETP (20 μM) or DMSO (1:1000) for 4 h. (**C**) Effects of PRL-3 stable overexpression on TIF formation. WI38 cells were analyzed by IF-FISH staining of pATM (green) and telomere (red). Left, representative staining. Arrows, foci of TIFs. Scale bar, 5 μm. Right, quantification of cells with ≥5 TIFs. Mean ± SD of two independent experiments. $n > 60$ metaphase per single experiment. Student's *t*-test. (**D**) Effects of PRL-3 stable overexpression on dysfunctional telomere repair pathways. Upper, representative CO-FISH staining of WI38 cells. Metaphase cells were stained with probes specific for leading (red) and lagging (green) strands and counterstained with DAPI (blue). Yellow arrow, a typical T-SCE. White arrow, a chromosome–chromosome fusion. Red arrowhead, a MTS. Scale bar, 2.5 μm. Lower, quantification of abnormalities. Mean ± SD of two independent experiments. $n > 1300$ chromosomes per single experiment. Student's *t*-test. (**E**) Southern blot analysis of PRL-3 stable overexpression-induced telomere deprotection. Genomic DNA from indicated cells were resolved on agarose gel, transferred to nitrocellulose membrane and probed with biotin-labeled telomere probe. (**F**) qPCR analysis of PRL-3 stable overexpression-induced telomere deprotection. Relative telomere to single copy gene (T/S) ratio of control cells was set as 1. Mean ± SD of three independent experiments. $n = 4$ replicates per single experiment. Student's *t*-test.

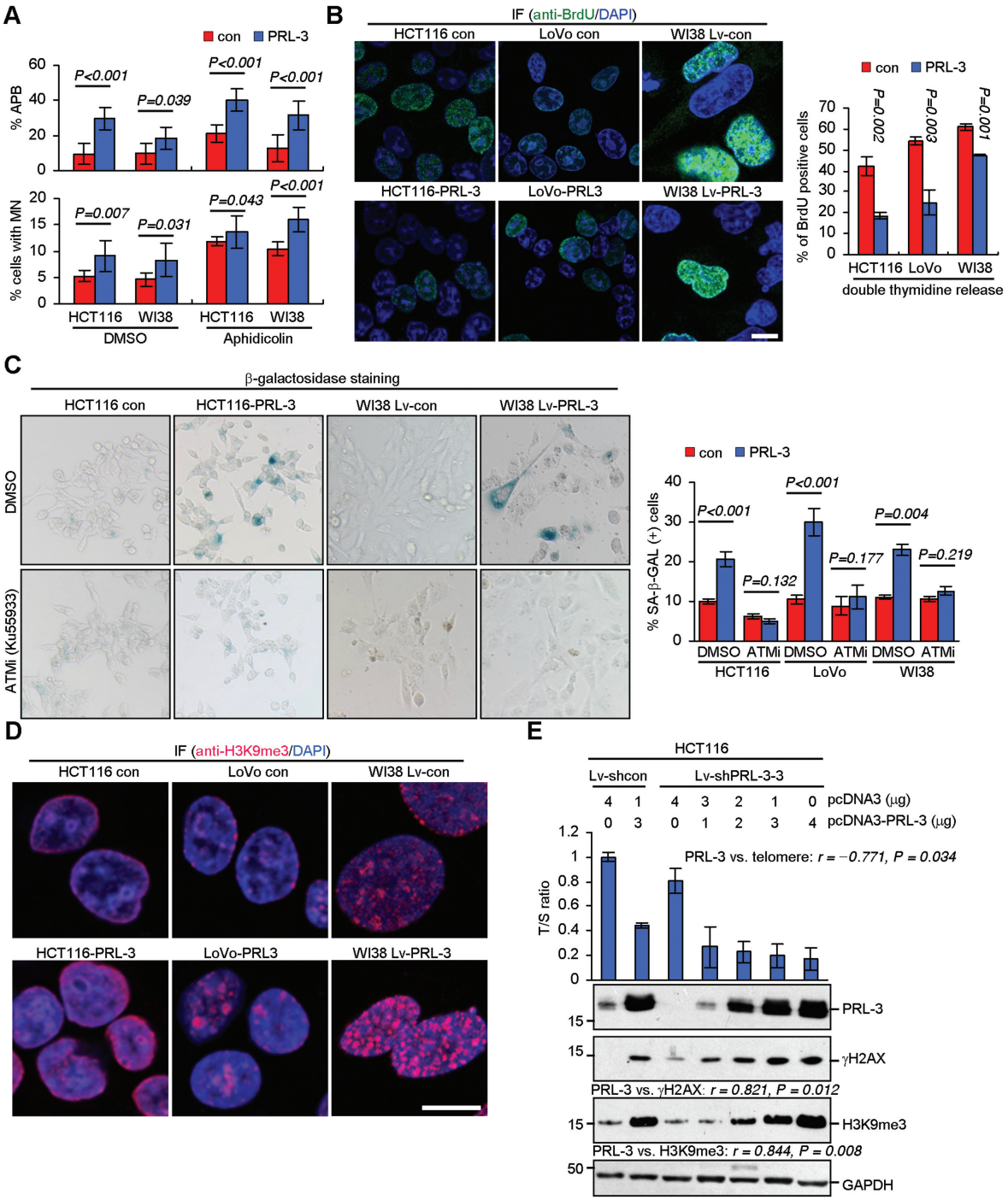

Figure 5. Overexpression of PRL-3 promotes chromosomal instability and senescence. (**A**) Effects of PRL-3 stable overexpression on APB and MN formation. Indicated cells were treated with aphidicolin (0.2 μM) or DMSO (1:1000) for 24 h, followed by DAPI staining. Mean ± SD of two independent experiments. Student's *t*-test. $n > 1500$ cells scored per sample for MN or $n > 60$ anaphase cells scored per sample for APB. (**B**) Effects of PRL-3 stable overexpression on BrdU incorporation. Indicated cells were treated with double-thymidine block, released into fresh medium containing 10 μM BrdU and incubated for 45 min. Cells were fixed, immunostained with anti-BrdU (green), and counterstained with DAPI (blue). Left, representative staining of BrdU. Scale bar, 15 μm. Right, quantification of BrdU-positive cells. Mean ± SD of two independent experiments. $n > 300$ cells per single experiment. Student's *t*-test. (**C**) Effects of PRL-3 stable overexpression on senescence. Indicated cells were treated with DMSO (1:1000) or Ku55933 (5 μM) for 24 h, followed by β-galactosidase staining. Left, representative staining. Right, quantification of β-galactosidase positive cells. Mean ± SD of three independent experiments. $n > 500$ cells per single experiment. Student's *t*-test. (**D**) Effects of PRL-3 stable overexpression on H3K9me3 levels. Indicated cells were fixed, immunostained with anti-H3K9me3 (red), and counterstained with DAPI (blue). (**E**) Effects of reconstituted PRL-3 on telomere length, DNA damage and senescence in PRL-3 stable knockdown cells. HCT116 control and PRL-3 stable knockdown cells were co-transfected with indicated amount of pcDNA3 and pcDNA3-PRL-3 plasmids. The total amount of plasmids for each sample was adjusted to 4 μg. After 72 h, protein lysates were subjected to western blot of PRL-3, γH2AX, H3K9me3 (lower). Genomic DNA was used for qPCR analysis of telomere length (upper). Protein bands were scanned and relative OD was calculated by normalizing to GAPDH. T/S ratio of HCT116 control cells transfected with pcDNA3 was set as 1. Pearson $\chi 2$ test.

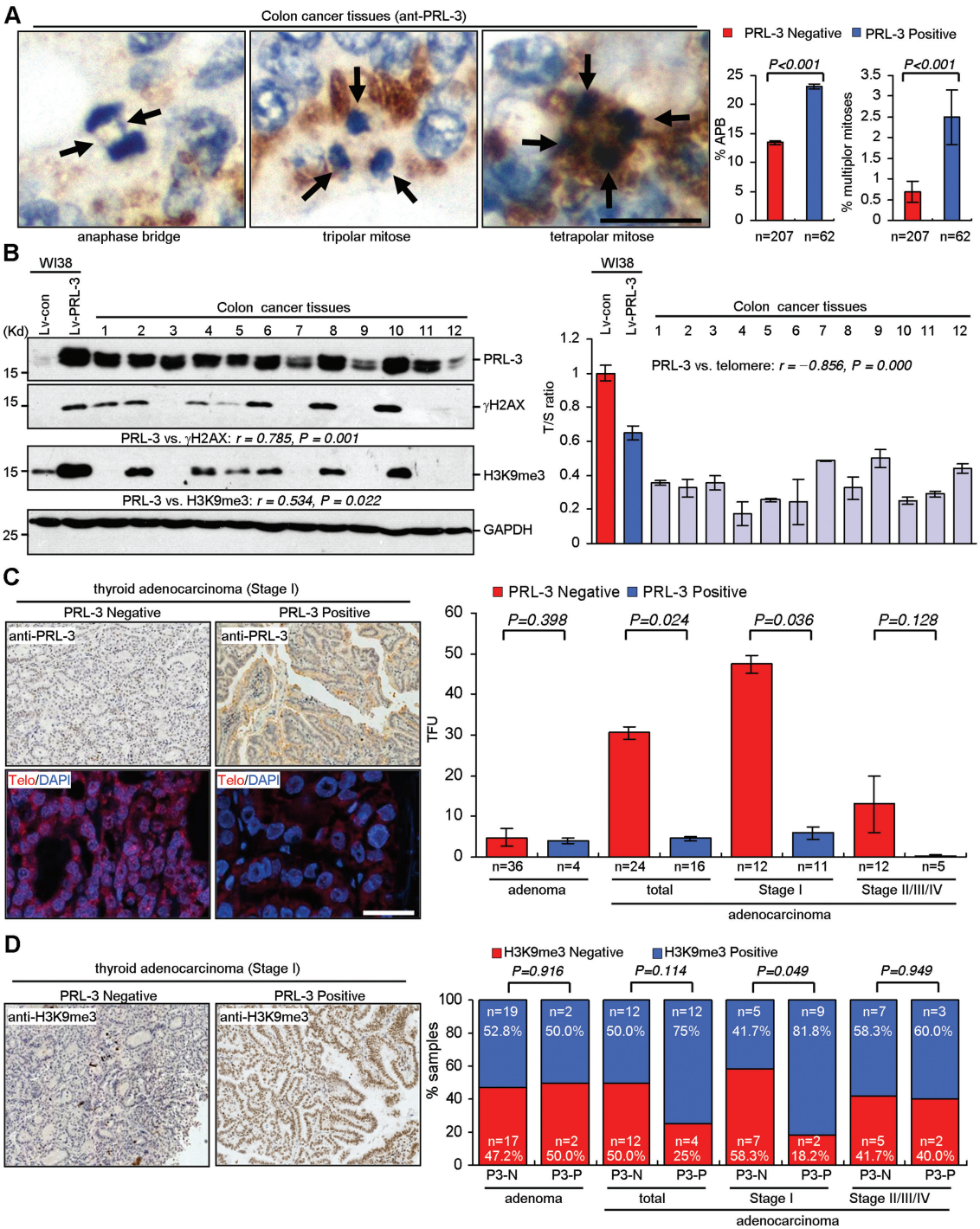

Figure 6. Correlations of PRL-3 with telomere length, chromosomal instability and senescence in clinical samples. (**A**) Correlations of PRL-3 with hallmarks of chromosomal instability in colon cancer tissues. Left, representative images of chromosomal mis-segregations (black arrows) in colon cancer tissues stained with an anti-PRL-3 mAb (brown areas). Scale bar, 20 μm. Right, percentage of anaphase cells with bridges and percentage of mitotic cells with ≥3 spindle poles in colon cancer tissues with negative and positive PRL-3 expression. Pearson $\chi 2$ test. (**B**) Correlations of PRL-3 with telomere length, DNA damage and senescence in colon cancer tissues. Protein lysates from 12 colon cancer tissues were subjected to western blot of PRL-3, γH2AX, H3K9me3 (left). Genomic DNA from these samples was used for qPCR analysis of telomere length (right). Protein lysates and genomic DNA from control and PRL-3 stable expressing WI38 cells were also compared. Protein bands were scanned and relative OD was calculated by normalizing to GAPDH. T/S ratio of WI38 control cells was set as 1. Pearson $\chi 2$ test. (**C**) Correlation of PRL-3 with telomere length in thyroid tissues. Left, representative images of PRL-3 immunohostochemical staining and telomere staining in thyroid adenocarcinoma (Stage I). Scale bar, 50 μm. Right, quantification of telomere fluorescence units (TFUs) in PRL-3 negative and positive samples. Results represent the average TFU ± SD. $n > 300$ nuclei scored per sample. Student's *t*-test. (**D**) Correlation of PRL-3 with senescence in thyroid tissues. Left, representative images of H3K9me3 immunostaining in thyroid adenocarcinoma (Stage I) with negative or positive PRL-3 expression. Right, analysis of correlation between PRL-3 and H3K9me3 status. P3-N, PRL-3 negative. P3-P, PRL-3 positive. Pearson $\chi 2$ test.

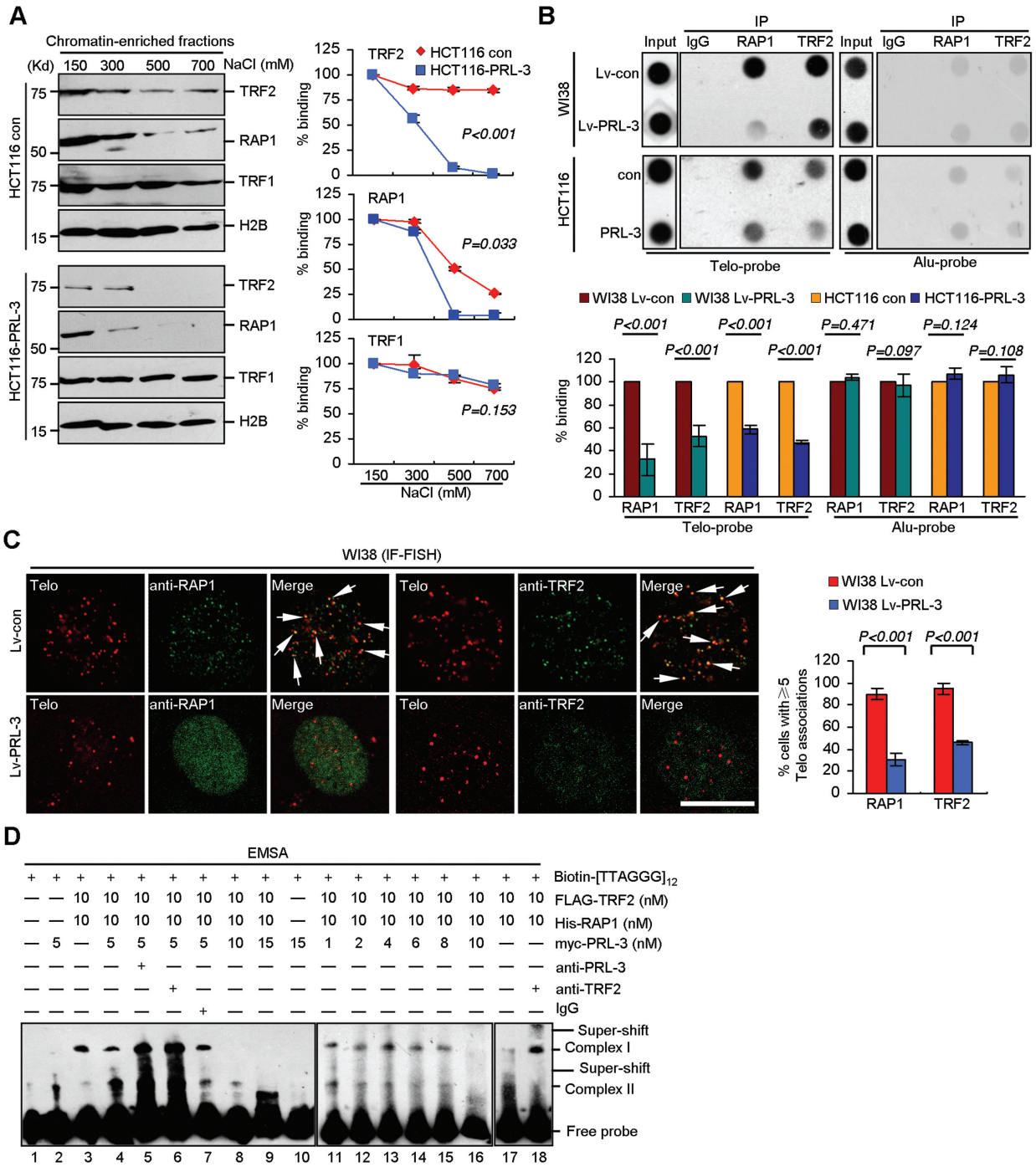

Figure 7. PRL-3 relocates RAP1 and TRF2 from telomeric DNA. (**A**) Effects of PRL-3 stable overexpression on the chromatin abundance of RAP1, TRF2 and TRF1. Nuclei from HCT116 cells were homogenized in buffer containing indicated concentrations of NaCl. Chromatin-enriched fractions were analyzed by western blot. Left, representative blots. Right, relative levels of TRF2, RAP1 and TRF1. Protein band were scanned and relative OD was calculated by normalizing to OD of H2B. The relative OD of sample prepared with 150 mM NaCl was set as 100%. Mean ± SD of three independent experiments. ANOVA. (**B**) Effects of PRL-3 stable overexpression on bindings of RAP1 and TRF2 to telomeric and Alu DNA. Indicated cells were crosslinked, immunoprecipitated with antibodies to RAP1, TRF2 or pre-immune IgG, and precipitated DNA was analyzed by ChIP. Upper, representative blots. Lower, quantification of relative OD, which was calculated by normalizing to that of Input. Relative OD of control was set as 100%. Mean ± SD of three independent experiments. Student's *t*-test. (**C**) Effects of PRL-3 stable overexpression on telomere associations of RAP1 and TRF2 in WI38 cells. Left, representative IF-FISH staining of telomere (red) and RAP1 or TRF2 (green). Arrows, foci of co-localization. Scale bar, 10 μm. Right, quantification of cells with ≥5 associations between RAP1 or TRF2 foci and telomere. Mean ± SD of two independent experiments. $n > 80$ cells per single experiment. Student's *t*-test. (**D**) EMSA analysis of PRL-3, RAP1 and TRF2's associations with telomeric DNA. Indicated concentrations of purified FLAG-TRF2, His-RAP1, myc-PRL-3 were co-incubated with Biotin-labeled telomere probe (20 nM). To induce super-shift, 0.1 μg anti-PRL-3 (lane 5), anti-TRF2 (lanes 6 and 18) and IgG (lane 7) were used. Note that anti-PRL-3 and anti-TRF2-induced super-shifts of Complex II partially co-migrated with Complex I (lanes 5 and 6).

shifts of Complex II (Figure 7D, lanes 5 and 6), suggesting that Complex II contained both TRF2 and PRL-3. Control IgG had no capacity to induce super-shift (Figure 7D, lane 7). Surprisingly, anti-TRF2 induced super-shift of Complex I was barely detectable in the presence of PRL-3 (Figure 7D, compare lanes 6 and 18). Increasing the amount of PRL-3 did not increase the Complex II, but resulted in disappearance of both Complex II and Complex I (Figure 7D, lanes 8–9). By titration, we found that ∼1:1 mole ratio of PRL-3 to TRF2–RAP1 could totally abolish binding of the latter complex to telomeric DNA (Figure 7D, lanes 11–16). The emergence of Complex II and the inhibitory effect of PRL-3 on anti-TRF2-induced super-shift of Complex I suggest that PRL-3 could alter the oligomeric state or the conformation of TRF2–RAP1 complex (please see 'Discussion' section). We then concluded that PRL-3 could promote dissociations of TRF2 and RAP1 from telomeric DNA *in vitro* and in cultured cells.

Disruption of PRL-3–RAP1 complex or expression of ectopic TRF2 attenuates PRL-3-promoted telomere deprotection and senescence

To ascertain whether PRL-3-promoted telomere deprotection, chromosomal instability, DNA damage response and senescence might be the results of PRL-3-imposed TRF2–RAP1 dissociation from telomeric DNA, we transiently overexpressed GFP-tagged Myb domain (Figure 8A), which could block recruitment of PRL-3 to RAP1–TRF2 complex (Figure 1H). GFP-Myb counteracted CHK1 phosphorylation (Figure 8A), telomere deprotection (Figure 8B), micronuclei formation (Figure 8C) and senescence (Figure 8D) in HCT116 cells stably overexpressing PRL-3. We noticed that GFP-Myb markedly decreased PRL-3-promoted cell migration (Figure 8E), underscoring the putative contribution of PRL-3-RAP1-TRF2 complex to PRL-3-regulated cell invasiveness. Changes in cell migration were associated with lowered phosphorylation of p65/RelA subunit of NFκB by GFP-Myb (Figure 8A), which was consistent with role of RAP1 in mediating PRL-3-induced NFκB activation (10).

Overexpression of TRF2 in cancerous tissues has been reported (34,84). To evaluate the influence of TRF2 on PRL-3-related effects, we used lentivirus-mediated expression of TRF2. Ectopic TRF2 alleviated PRL-3-promoted CHK1 phosphorylation (Figure 8F), telomere deprotection (Figure 8G), micronuclei formation (Figure 8H), and senescence (Figure 8I), emphasizing the involvement of TRF2 in PRL-3′s effects. We found PRL-3-induced cell migration was further boosted by TRF2 (Figure 8J), which was in agreement with TRF2′s non-telomeric functions in promoting malignant phenotypes of cancer cells (30,84). Overexpression of TRF2 in HCT116 control cells decreased telomere length (Figure 8G), which was consistent with results of previous studies using fibroblasts (84,85).

PRL-3-promoted telomere dysfunction and senescence are associated with colon tumorigenesis in mice

To further assess the physiological relevance of PRL-3 gain-of-function, we generated C57BL/6J mice transgenic (TG) for murine *PRL3* with an inducible expression system (Supplementary Figure S7A and B). Upon treatment with DOX for 8 weeks, PRL-3 was induced in the colon and liver tissues (Figure 9A and Supplementary Figure S7C). Immunohistochemical staining validated PRL-3 expression in colon tissues (Figure 9B). Induction of PRL-3 at protein levels was not as robust as transcript levels (Figure 9A). The unparalleled transcript and protein levels of PRL-3 was discovered previously, likely due to PolyC-RNA-binding protein 1 (PCBP1)-mediated suppression of PRL-3 translation (23). By using lysates from HCT116 cells overexpressing PRL-3 as the reference, we found level of PRL-3 in colon tissue of wild-type animal was similar to the endogenous PRL-3 in HCT116 cells, and the level of induced PRL-3 in TG mouse was similar to the myc-PRL-3 (Figure 9A). Thus, PRL-3 induction in transgenic animal is comparable to cultured colon cancer cells stably overexpressing PRL-3. *PRL3*-deletion decreased the body mass of male mice (21), while the increase in body mass of both genders of *PRL3*-TG mice was higher than that of wild-type mice during DOX treatment (Supplementary Figure S7D). PRL-3 overexpression was shown to promote ERK1/2 phosphorylation in cancer cell lines (11,13,15). We also found elevated ERK1/2 phosphorylation in the colon tissues after DOX treatment (Figure 9C). Although *PRL3*-TG mice did not exhibit overt developmental defects or structural abnormality in the colon after DOX induction (Figure 9B), stronger H3K9me3 staining was observed (Supplementary Figure S7E), confirming the pro-senescent capacity of PRL-3 in mice. Transcription of senescence-associated secretory phenotype-associated factors (28,29), including TGF-β, TNF-α, COX2, Occludin and CXCL1, was elevated in colon tissues of *PRL3*-TG mice (Supplementary Figure S7F). Importantly, FISH staining revealed that *PRL3*-TG correlated with decreased telomere signals in colon tissues (Figure 9D). Southern blot and qPCR assays further showed telomere deprotection in colon and liver tissues of *PRL3*-TG mice (Figure 9E and F). These results confirmed the ability of PRL-3 to promote telomere deprotection *in vivo*. Following DOX treatment for 8 weeks, chronic inflammation was induced in mice by 4 cycles of DSS treatment. Histological evaluation found that adenocarcinoma was developed in 5/7 of *PRL3*-TG mice and 1/8 of wild-type mice (Figure 9G), suggesting that *PRL3*-TG promotes inflammation-related colon malignancy. More anaphase bridges were detected in colon tumor tissues of *PRL3*-TG mice (Figure 9H), supporting the notion that chromosomal mis-segregation is associated with *PRL3*-TG-promoted tumorigenesis. There were increased TUNEL positive cells in colon tumor tissues of *PRL3*-TG mice (Supplementary Figure S7G). Moreover, levels of caspase-3 cleavage, γH2AX, and H3K9me3 expression were also elevated in colon tumor tissues of *PRL3*-TG mice (Figure 9I). Thus, *PRL3*-TG-promoted tumorigenesis is associated with enhanced DDR, apoptosis and senescence, which is consistent with the role of chronic inflammation-induced DDR in colon tumorigenesis of mice (86,87).

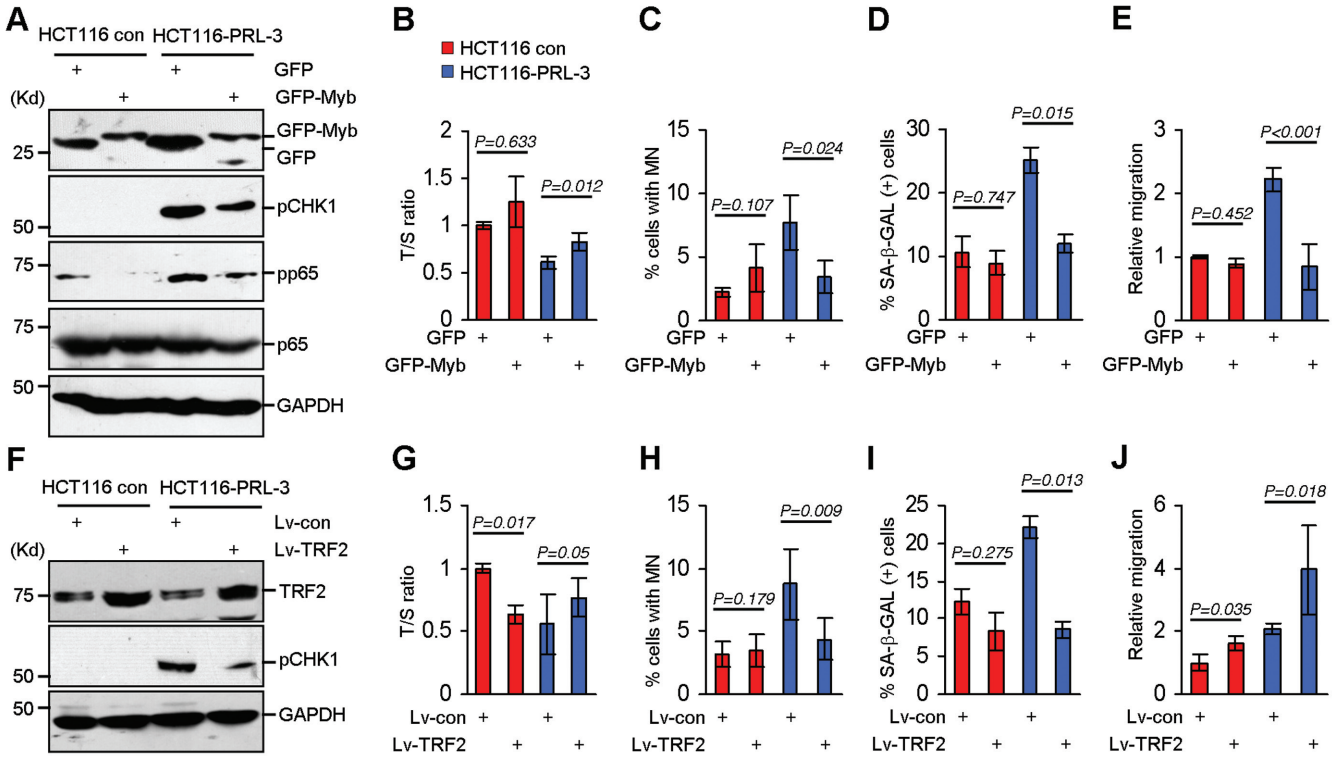

Figure 8. Disrupting PRL-3-RAP1 complex or expressing ectopic TRF2 attenuates PRL-3 overexpression-promoted telomere deprotection, DNA damage, chromosomal instability and senescence. (**A**) HCT116 control and PRL-3 overexpressing cells were transfected with 0.5 μg of pEGFP-N1-Myb or pEGFP-N1 plasmid for 72 h, and indicated proteins were analyzed by western blot. (**B**) qPCR analysis of telomere length of cells in (A). T/S ratio of HCT116 control cells transfected with pEGFP-N1 was set as 1. Mean ± SD of three independent experiments. Three replicates per single experiment. Student's *t*-test. (**C**) Quantification of micronuclei of cells in (A). Mean ± SD of two independent experiments. $n > 500$ cells per single experiment. Student's *t*-test. (**D**) Quantification of β-galactosidase-positive cells in (A). Mean ± SD of two independent experiments. $n > 300$ cells per single experiment. Student's *t*-test. (**E**) Relative migration of cells in (A). Cells were allowed to migrate through transwell chambers for 24 h. Value of HCT116 control cells transfected with pEGFP-N1 was set as 1. Mean ± SD of two independent experiments. Three replicates per single experiment. Student's *t*-test. (**F**) HCT116 control and PRL-3 overexpressing cells were infected with control (Lv-con) or TRF2-expressing lentivirus (Lv-TRF2) for 120 h, and lysates were subjected to western blot. (**G**) qPCR analysis of telomere length of cells in (F). T/S ratio of HCT116 control cells infected with Lv-con was set as 1. Mean ± SD of three independent experiments. 3 replicates per single experiment. Student's *t*-test. (**H**) Quantification of micronuclei of cells in (F). Mean ± SD of three independent experiments. $n > 500$ cells per single experiment. Student's *t*-test. (**I**) Quantification of β-galactosidase-positive cells in (F). Mean ± SD of three independent experiments. $n > 300$ cells per single experiment. Student's *t*-test. (**J**) Relative migration of cells of (F). Cells were allowed to migrate through transwell chambers for 24 h. Value of HCT116 control cells infected with Lv-con was set as 1. Mean ± SD of three independent experiments. Three replicates per single experiment. Student's *t*-test.

DISCUSSION

In this study, we identified PRL-3 as a telomere-associated protein which is assisted by shelterin components RAP1 and TRF2. We further revealed two facets of PRL-3: (i) PRL-3 loss-of-function has no effects on telomere integrity or chromosomal stability, but promotes DDR and senescence in a ROS-dependent manner, and (ii) PRL-3 gain-of-function induces telomere dysfunction, DDR, chromosomal instability and senescence, which are associated with removal of RAP1 and TRF2 from telomeric DNA.

Distinctions in the consequences of PRL-3 loss-of-function and gain-of-function suggest that PRL-3 level should be precisely controlled to maintain the telomere function and chromosomal stability. Several factors, such as STAT5, STAT3 and TGF-β could transcriptionally regulate PRL-3 expression (9,15,88). Additionally, PCBP1-mediated translational suppression results in un-paralleled mRNA and protein levels of PRL-3 in human and mouse cells (23). It was recently found that deubiquitinating enzyme USP4 promotes PRL-3 stabilization in colon cancer cells (89). Therefore, PRL-3 expression is regulated at multiple layers. Some of these factors possess pro-senescent capacity and their deregulations are closely linked to tumorigenesis (28,29). Thus, whether PRL-3 and PRL-3-induced telomere dysfunction have some contributions to the effects of these factors deserves future investigation.

We evaluated the effects of PRL-3 gain-of-function by using cultured cell overexpressing PRL-3, clinical samples with varying levels of PRL-3 and mice transgenic for PRL-3. We stably overexpressed myc-tagged PRL-3 in human colon cancer cells. It was recently reported that His6-tag may yield potential influences on protein functions and interaction properties (90,91). We found that myc-PRL-3 and endogenous PRL-3 had similar distribution pattern in different subcellular fractions. In addition, the myc-PRL-3 protein could associate with both RAP1 and telomeric DNA, suggesting that the interaction profile of myc-PRL-3 is similar to that of endogenous PRL-3. To further exclude

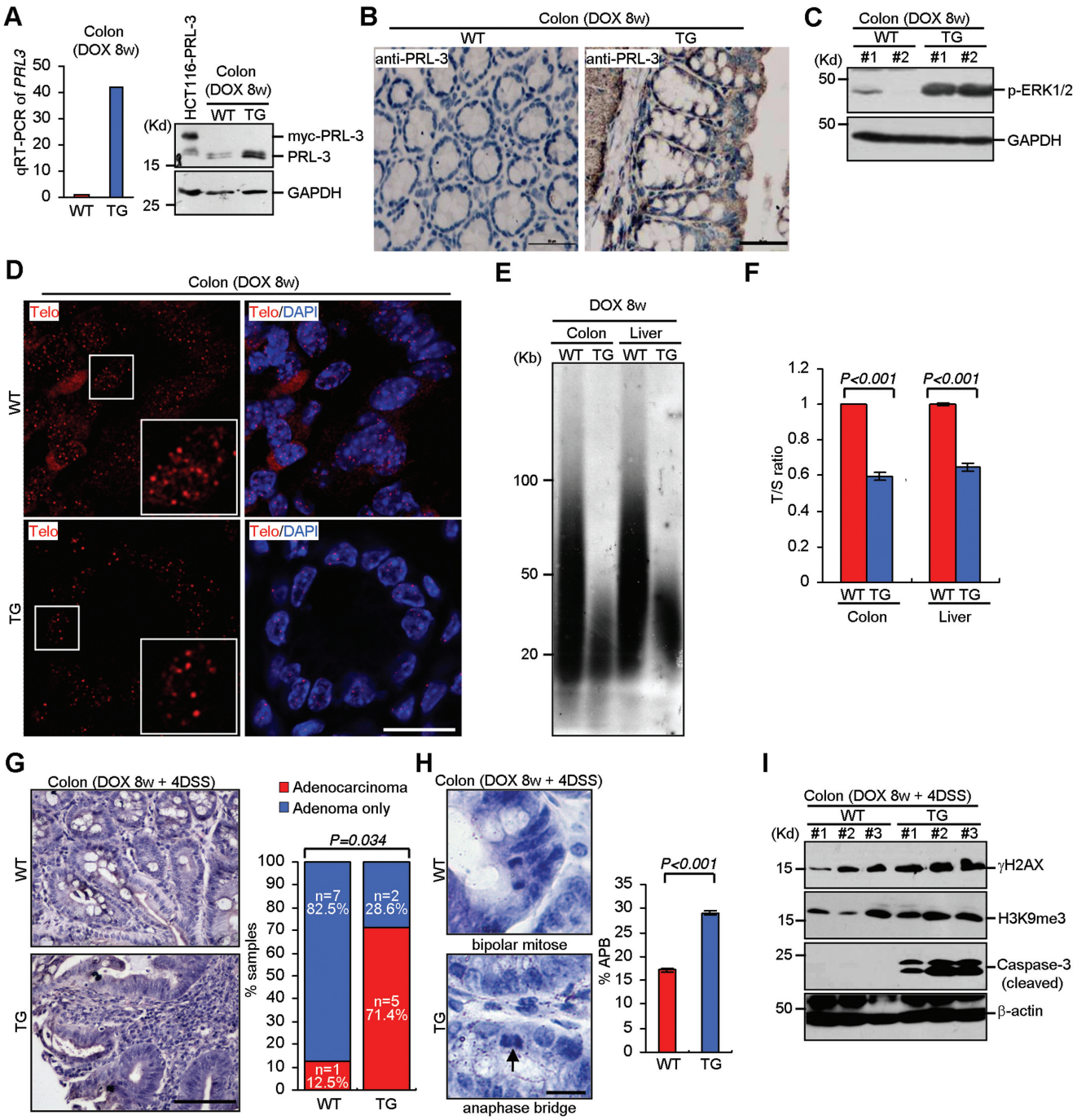

Figure 9. PRL-3-promoted telomere deprotection is associated with colon tumorigenesis in mice. (**A**) qRT-PCR (left) and western blot (right) analysis of PRL-3 expression in distal colon tissues of wild-type (WT) and transgenic (TG) mice treated with DOX for 8 weeks. Lysates from HCT116 cells stably overexpressing PRL-3 were used as the control. (**B**) Representative immunohistochemical staining of PRL-3 (brown areas) in distal colon tissues of mice treated with DOX for 8 weeks. Sections were counterstained with Hematoxylin and eosin (HE). Scale bar, 50 μm. (**C**) PRL-3-induced ERK1/2 phosphorylation in distal colon tissues of mice ($n = 2$) treated with DOX for 8 weeks. (**D**) Representative FISH staining of telomere in distal colon tissues of mice treated with DOX for 8 weeks. Scale bar, 50 μm. (**E**) Southern blot analysis of telomere length in distal colon and liver tissues of mice treated with DOX for 8 weeks. (**F**) qPCR analysis of telomere length in distal colon and liver tissues of mice treated with DOX for 8 weeks. T/S ratio of WT mice was set as 1. Mean ± SD of three independent experiments. $n = 3$ mice per single experiment. Student's test. (**G**) PRL-3-promoted colon malignancy in mice. Mice were treated with DOX for 8 weeks, followed by four cycles of DSS administration. Tumors were microscopically analyzed at the end of the 4th DSS cycle and classified as adenocarcinoma or adenoma. Left, representative images of HE-stained colon tumors. Scale bars, 100 μm. Right, incidence of adenocarcinoma or adenoma in WT ($n = 8$) and TG ($n = 7$) mice. Pearson $\chi 2$ test. (**H**) PRL-3-promoted chromosomal mis-segregation in colon tumor tissues at the end of the 4th DSS cycle. Left, representative images of normal (in WT) and abnormal (in TG) mitoses. Arrow, an anaphase bridge. Scale bars, 25 μm. Right, incidence of anaphase bridge in WT ($n = 8$) and TG ($n = 7$) mice. Pearson $\chi 2$ test. (**I**) Expression of indicated proteins in the distal colon tissues ($n = 3$) at the end of the fourth DSS cycle.

potential interference of myc-tag, we stably overexpressed untagged PRL-3 in WI38 fibroblasts. It was revealed that myc-PRL-3 and untagged PRL-3 had similar impacts on inducing DNA damage response, TIF formation, telomere deprotection, induction of chromosomal stability, promotion of senescence and inhibiting TRF2 and RAP1 binding to telomeric DNA. Therefore, effects resulting from PRL-3 overexpression are irrespective of the presence of tag or types of cell.

For clinical samples, we used archived colon cancer sections and thyroid tissue arrays. With these samples, we confirmed the inverse correlation of PRL-3 with telomere length (for thyroid adenocarcimoma) as well as its positive correlations with senescence (for Stage I thyroid adenocarcimoma) and chromosomal instability (for colon cancer). We also used freshly dissected colon cancer tissues and verified correlations of PRL-3 with telomere length, senescence and DNA damage response. In the same assay, we found that PRL-3 levels in some of these tissues were comparable with overexpressed PRL-3 of WI38 fibroblasts. We therefore propose that, to some extent, PRL-3 expression in colon cancer tissues could be simulated by overexpression in cultured cells. As for mice transgenic for PRL-3, we further confirmed the effects of PRL-3 on inducing telomere deprotection and senescence, and importantly, demonstrated PRL-3′s stimulatory effect on promoting inflammation-related colon malignancy. We noticed that PRL-3 level in colon tissues of transgenic animal is comparable to cultured colon cancer cells stably overexpressing PRL-3; thus, PRL-3 transgene could also be simulated by overexpression in cultured cells.

The previously described results were mainly correlative. Considering that PRL-3 has pleiotropic effects on cells through the engagement with diverse signaling pathways (9–19), it is imperative to show that the adverse impact of PRL-3 on telomeres is due to dissociated RAP1–TRF2 complex from telomeric DNA. To this end, we perform gel shift assay and showed diminished bindings of TRF2 and RAP1 to telomeric DNA upon addition of PRL-3. We used equal moles of TRF2 and RAP1 for the *in vitro* assay, based on the reported ∼1:1 mole ratio between TRF2 and RAP1 in cells (92). The concentrations of TRF2 and RAP1 were set as 10 nM, which was similar to recently calculated cellular concentration of free shelterin complexes (∼7 nM) (93). However, the concentration of PRL-3 in the nucleus is unclear. Thus, whether the concentrations of PRL-3 used for *in vitro* assay could reflect endogenous PRL-3 in natural physiological or pathological conditions is also required to be assessed in future studies.

Nevertheless, we provided direct evidence to demonstrate that PRL-3 indeed has a capacity to inhibit the telomere-binding activities of TRF2 and RAP1. A critical issue raised by our study is how PRL-3 removes RAP1 and TRF2 from telomeres. We found that incorporation of PRL-3 did not decrease, but increased the mobility of Complex II, implying the alteration in oligomeric state or/and conformation of TRF2/RAP1. TRF2 binds to telomeric DNA through homodimerization (37); however, several groups have reported oligomerization of TRF2 (37,45,94–98). Oligomerization may further promote binding of TRF2 to telomeric DNA (37) and favor the formation of T-loop structure (94–96). In addition, RAP1 oligomerization was observed (97). As calculated, TRF2 and RAP1 form a 4:4 complex (97). Formation of this high order multimeric complex may be important for telomere function and end protection (97). Based on these considerations, faster mobility of Complex II could be due to decreased oligomeric state of RAP1 or/and TRF2 in the presence of PRL-3. It should be mentioned that PRL-3 was also found to be partially dimerized (99). Because of relatively low molecular weight of PRL-3 (∼20 K_d), incorporation of PRL-3 would be not sufficient to compensate for the lowered oligomeric state of RAP1 or/and TRF2. However, this hypothesis needs to be validated in future studies. It is intriguing that anti-TRF2 failed to induce obvious super-shift of Complex I in the presence of PRL-3. This effect could be due to PRL-3-induced conformational change of TRF2 in Complex II, making the anti-TRF2 preferentially recognizes TRF2 of Complex II, but not that of Complex I. Despite that no obvious effects of RAP1 on TRF2 binding to telomeres were observed in cells (32,46), some studies disclosed that RAP1 has an intriguing ability to control TRF2 recognition of telomeric DNA in the *in vitro* systems (97,100). A recent study proposed a model in which RAP1-mediated changes in conformation and function of TRF2, and *vice versa* (98). Furthermore, this model predicted that TRF2–RAP1 complex could adopt alternative open or closed conformation, depending on the presence or absence of binding partners (98). Considering that PRL-3 is a RAP1 binding protein and the potential of PRL-3 to inhibit the association of TRF2–RAP1 with telomeric DNA, it will be interesting to evaluate the effect of PRL-3 on the conformation of TRF2–RAP1 complex. In addition to telomere localization, there is a pool of free shelterin components in the nucleoplasma and cytoplasma, as uncovered by several studies (32,35,48,92). Through subcellular fractionation, we also detected co-existence of PRL-3, RAP1 and TRF2 in the nucleoplasma in HCT116 cells overexpressing PRL-3. Hence, the possibility that nucleoplasmic retention of PRL-3–RAP1–TRF2 complex may restrict the recruitment of TRF2–RAP1 complex to telomeric DNA could not be fully discounted.

PRL-3 overexpression promoted adverse effects on telomere could be explained by the removal of TRF2–RAP1 from telomeric DNA, because these effects were counteracted by re-introduction of TRF2 or disruption of PRL-3–RAP1–TRF2 complex. However, we could not exclude the involvement of other mechanism(s). We identified Myb domain of RAP1 to be crucial for its association with PRL-3. A recent study showed the pivotal role of this domain in preventing telomere loss and fusion (52). We also detected these two types of telomere abnormality in both WI38 and HCT116 cells overexpressing PRL-3. Whether PRL-3 could further generate damage to telomere through its association with Myb domain of RAP1 will be an interesting topic. Accumulating evidence has demonstrated the participation of repair factors and signaling proteins in the telomere maintenance (31). Of note, PRL-3 overexpression promoted telomere loadings of 53BP1 and RAD51, which respectively promote NHEJ and HDR, and play essential roles in DNA repair and genomic stability (31,53,83). Although the mechanism whereby PRL-3 in-

creased 53BP1 and RAD51 recruitment remains to be answered, our present study suggests that gain-of-function of PRL-3 may disrupt telomere integrity and chromosomal stability through diverse pathways.

Shelterin could form the six-component multimeric complex, however, the existence of sub-complexes containing fewer components has been revealed by biochemical fractionation of HeLa cell nuclear extracts (101–103), *in vitro* binding assays (93,104) and analysis of cells deficient for one or more shelterin components (32,49,64,105–108). These studies shed light on the requirement of individual components in the telomere assembly of shelterin complex and sub-complexes. Because only TRF1 and TRF2 could associate with ds-telomeric DNA (31), and the ss-telomeric DNA binding activity of POT1 is not required for the telomere localization of itself (64) or the other shelterin proteins (109), the recruitment of shelterin complex and sub-complexes to telomeric DNA is mediated by TRF1 and TRF2 (31,32,93,104). Quantitative analysis of shelterin abundance in HeLa1.3 and HTC75 cells found high copy numbers of TRF2/RAP1/TIN2, medium copy numbers of TRF1 and low copy numbers of TPP1/POT1 (92). It is possible to envisage high mole ratio of TRF2–RAP1 sub-complex to six-component whole complex or other sub-complexes. Unfortunately, the roles of distinct sub-complexes in telomere maintenance are poorly understood. In the present study, we did not detect association of PRL-3 with other four shelterin proteins in the pull-down assay with HCT116 cell lysates. Therefore, it's plausible that PRL-3 is preferentially recruited to the two-component sub-complex of TRF2–RAP1. This prediction is partially supported by the following results: not all of RAP1 foci, TRF2 foci or telomere foci were positive for PRL-3 in IF and IF-FISH analysis, and ∼30 to ∼60% telomeric DNA remained positive for RAP1 or TRF2 in PRL-3 overexpressing cells as assayed by Telo-ChIP. Based on recently proposed 3D assembly mechanism, different shelterin sub-complexes operate independently and could quickly cover unprotected telomere repeats to maintain genome integrity (93). Thus, we speculate that, unlike the conditions of deletion of TRF2 (106,107) or expression of dominant negative TRF2 (TRF2ΔBΔM) (64,105), which strongly affected the telomere-binding of shelterin components, while the cellular level of TRF2 was stable in cells overexpressing PRL-3, a subset of telomere-bound TRF2–RAP1 might belong to compensated whole complex and/or other sub-complexes. This speculation is partly supported by the increased telomere-bound TIN2/TPP1/POT1 in HCT116 cells overexpressing PRL-3. The concomitant increment of telomere-bound TIN2/TPP1/POT1 was also consistent with their close physical and functional associations (103,110,111). For example, TPP1 and POT1 were disappeared from telomeres upon TIN2 deletion (110). Deficiency of RNF8, a positive regulator of TPP1, could significantly decrease telomere-bound TPP1/TIN2/POT1, while that of TRF2/RAP1/TRF1 remained stable (111). PRL-3 overexpression did not affect levels of telomere-associated TRF1 or chromatin-bound TRF1. Although structurally similar, TRF1 and TRF2 were shown to exploit different mechanisms to recognize ds-telomeric DNA (104,112,113). Expression of TRF2ΔBΔM in human cells did not change level of telomere-bound TRF1 (64,105). Moreover, telomere-bound TRF1 was not affected by deletion of TRF2 in MEF cells (106,107). In MEF cells expressing TRF2 with temperature-sensitive (ts) mutation in the DNA-binding domain, the telomere association of TRF1 was reduced at non-permissive temperature (108). Thus, except for the system of TRF2(ts) mutation, telomere-localization of TRF1 was not affected by expression of TRF2ΔBΔM or TRF2 deficiency, suggesting a stable telomere binding activity of TRF1 upon TRF2 loss. Such characteristic of TRF1 may, at least in part, explain its relatively steady telomere association in response to PRL-3-induced removal of TRF2 from telomeric DNA.

Telomeric DNA is vulnerable to oxidative modification because of the intrinsic G-rich sequences (114). Oxidative stress triggers telomeric DNA damage, telomere shortening, telomere dysfunction and promotes cellular senescence (115,116). Oxidative stress could also disrupt telomeric DNA binding activities of TRF1 and TRF2 *in vitro* (117). We found that PRL-3 silencing induced DNA damage response and senescence in a ROS-dependent fashion, but had no obvious effect on telomere integrity. We used three approaches to examine damages to telomere: IF-FISH assay of TIF formations, counting the ratios of anaphase bridges and micronuclei, and measuring the telomere length. PRL-3 silencing did not affect the levels of TIF, micronuclei and anaphase bridges. Additionally, PRL-3 silencing had no influence on telomere length. Therefore, although the mechanism underlying PRL-3 silencing-induced oxidative stress remains to be clarified, such stress is mild and inadequate to produce telomeric DNA damage. Contrary to PRL-3 overexpression-induced TRF2 dissociation from telomere, PRL-3 silencing did not increase telomere loading of TRF2 in the ChIP analysis. Previously, stoichiometric analysis of six shelterin components in cancer cells demonstrated high copy numbers of RAP1 and TRF2 (92). It's plausible that HCT116 and SW480 cells used in our present study expressed high copy number of TRF2 that already occupied the telomeric DNA, meanwhile there was only a small subset of telomeres co-localized with PRL-3. Thus, silencing of PRL-3 could not globally increase the amount of telomere-bound TRF2. However, to precisely evaluate the influence of PRL-3 silencing on telomere localization of TRF2 in cells, more efforts are required. We did observe that PRL-3 silencing caused low telomere binding of RAP1 in the ChIP assay, likely due to the stimulatory role of PRL-3 in transcriptional activation of RAP1 (10). Accumulating evidence suggests that RAP1 is also required for telomere homeostasis in mammalian cells (47–53). However, PRL-3 silencing was not associated with overt telomere dysfunction. We reason that, because of high copy number of shelterin components occupied the telomeres (92), or/and the fast functioning of shelterin sub-complexes to maintain the shelterin density at telomeric DNA (93), loss of PRL-3-induced partial down-regulation of RAP1 is still inadequate to generate damages to telomeres.

The pro-invasive property of PRL-3 in cancer cells has been well demonstrated (1–3,11), and its essential role in promoting other malignant phenotypes was uncovered in recent years (9,12,15). By showing that overexpression of PRL-3 could promote telomere dysfunction, DNA damage

response, chromosomal instability and senescence in both cultured cells and transgenic mice, our results provide new understanding of the role of PRL-3 in affecting genomic integrity. Because mice transgenic for PRL-3 had higher incidence of colon malignancy upon DSS treatment, PRL-3 may contribute to inflammation-related tumorigenesis. However, this assumption needs to be rigorously verified by assessing more human premalignant/malignant tissues and animal model systems in future experiments.

SUPPLEMENTARY DATA

Supplementary Data are available at NAR Online.

ACKNOWLEDGEMENTS

We deeply appreciate Junhua Zou (Peking University Health Science Center) for assistance in cytogenetic analysis, Bin Dong (Peking University Cancer Hospital & Institute) for assistance in pathological evaluation, Daochun Kong (College of Life Sciences of Peking University) for generous sharing of pulsed-field electrophoresis apparatus. We are very grateful to Namratha Sastry (Northwestern University) for critical reading of the manuscript.

FUNDING

National Natural Science Foundation of China [81230046, 81301747]; Ministry of Science and Technology of China [2015CB553906, 2013CB910504]. Funding for open access charge: National Natural Science Foundation of China [81230046, 81301747].
Conflict of interest statement. None declared.

REFERENCES

1. Al-Aidaroos,A.Q. and Zeng,Q. (2010) PRL-3 phosphatase and cancer metastasis. *J. Cell. Biochem.*, **111**, 1087–1098.
2. Bessette,D.C., Qiu,D. and Pallen,C.J. (2008) PRL PTPs: mediators and markers of cancer progression. *Cancer Metastasis. Rev.*, **27**, 231–252.
3. Rios,P., Li,X. and Köhn,M. (2013) Molecular mechanisms of the PRL phosphatases. *FEBS J.*, **280**, 505–524.
4. Achiwa,H. and Lazo,J.S. (2007) PRL-1 tyrosine phosphatase regulates c-Src levels, adherence, and invasion in human lung cancer cells. *Cancer Res.*, **67**, 643–650.
5. Hardy,S., Wong,N.N., Muller,W.J., Park,M. and Tremblay,M.L. (2010) Overexpression of the protein tyrosine phosphatase PRL-2 correlates with breast tumor formation and progression. *Cancer Res.*, **70**, 8959–8967.
6. Forte,E., Orsatti,L., Talamo,F., Barbato,G., De Francesco,R. and Tomei,L. (2008) Ezrin is a specific and direct target of protein tyrosine phosphatase PRL-3. *Biochim. Biophys. Acta*, **1783**, 334–344.
7. Mizuuchi,E., Semba,S., Kodama,Y. and Yokozaki,H. (2009) Down-modulation of keratin 8 phosphorylation levels by PRL-3 contributes to colorectal carcinoma progression. *Int. J. Cancer*, **124**, 1802–1810.
8. Tian,W., Qu,L., Meng,L., Liu,C., Wu,J. and Shou,C. (2012) Phosphatase of regenerating liver-3 directly interacts with integrin β1 and regulates its phosphorylation at tyrosine 783. *BMC Biochem.*, **13**, 22.
9. Al-Aidaroos,A.Q., Yuen,H.F., Guo,K., Zhang,S.D., Chung,T.H., Chng,W.J. and Zeng,Q. (2013) Metastasis-associated PRL-3 induces EGFR activation and addiction in cancer cells. *J. Clin. Invest.*, **123**, 3459–3471.
10. Lian,S., Meng,L., Liu,C., Xing,X., Song,Q., Dong,B., Han,Y., Yang,Y., Peng,L., Qu,L. *et al.* (2013) PRL-3 activates NF-κB signaling pathway by interacting with RAP1. *Biochem. Biophys. Res. Commun.*, **430**, 196–201.
11. Peng,L., Xing,X., Li,W., Qu,L., Meng,L., Lian,S., Jiang,B., Wu,J. and Shou,C. (2009) PRL-3 promotes the motility, invasion, and metastasis of LoVo colon cancer cells through PRL-3-integrin beta1-ERK1/2 and-MMP2 signaling. *Mol. Cancer*, **8**, 110.
12. Ye,Z., Al-Aidaroos,A.Q., Park,J.E., Yuen,H.F., Zhang,S.D., Gupta,A., Lin,Y., Shen,H.M. and Zeng,Q. (2015) PRL-3 activates mTORC1 in Cancer Progression. *Sci. Rep.*, **5**, 17046.
13. Walls,C.D., Iliuk,A., Bai,Y., Wang,M., Tao,W.A. and Zhang,Z.Y. (2013) Phosphatase of regenerating liver 3 (PRL3) provokes a tyrosine phosphoproteome to drive prometastatic signal transduction. *Mol. Cell. Proteomics*, **12**, 3759–3777.
14. Yang,Y., Lian,S., Meng,L., Qu,L. and Shou,C. (2017) Antibody array revealed PRL-3 affects protein phosphorylation and cytokine secretion. *PLoS One*, **12**, e0169665.
15. Park,J.E., Yuen,H.F., Zhou,J.B., Al-Aidaroos,A.Q., Guo,K., Valk,P.J., Zhang,S.D., Chng,W.J., Hong,C.W., Mills,K. *et al.* (2013) Oncogenic roles of PRL-3 in FLT3-ITD induced acute myeloid leukaemia. *EMBO Mol. Med.*, **5**, 1351–1366.
16. Zhou,J., Chong,P.S., Lu,X., Cheong,L.L., Bi,C., Liu,S.C., Zhou,Y., Tan,T.Z., Yang,H., Chung,T.H. *et al.* (2014) Phosphatase of regenerating liver-3 is regulated by signal transducer and activator of transcription 3 in acute myeloid leukemia. *Exp. Hematol.*, **42**, 1041–1052.
17. Zhang,C., Tian,W., Meng,L., Qu,L. and Shou,C. (2016) PRL-3 promotes gastric cancer migration and invasion through a NF-κB-HIF-1α-miR-210 axis. *J. Mol. Med.*, **94**, 401–415.
18. Chong,P.S., Zhou,J., Cheong,L.L., Liu,S.C., Qian,J., Guo,T., Sze,S.K., Zeng,Q. and Chng,W.J. (2014) LEO1 is regulated by PRL-3 and mediates its oncogenic properties in acute myelogenous leukemia. *Cancer Res.*, **74**, 3043–3053.
19. Liu,Y., Zheng,P., Liu,Y., Ji,T., Liu,X., Yao,S., Cheng,X., Li,Y., Chen,L., Xiao,Z. *et al.* (2013) An epigenetic role for PRL-3 as a regulator of H3K9 methylation in colorectal cancer. *Gut*, **62**, 571–581.
20. Maacha,S., Planque,N., Laurent,C., Pegoraro,C., Anezo,O., Maczkowiak,F., Monsoro-Burq,A.H. and Saule,S. (2013) Protein tyrosine phosphatase 4A3 (PTP4A3) is required for Xenopus laevis cranial neural crest migration in vivo. *PLoS One*, **8**, e84717.
21. Zimmerman,M.W., Homanics,G.E. and Lazo,J.S. (2013) Targeted deletion of the metastasis-associated phosphatase Ptp4a3 (PRL-3) suppresses murine colon cancer. *PLoS One*, **8**, e58300.
22. Cramer,J.M., Zimmerman,M.W., Thompson,T., Homanics,G.E., Lazo,J.S. and Lagasse,E. (2014) Deletion of Ptp4a3 reduces clonogenicity and tumor-initiation ability of colitis-associated cancer cells in mice. *Stem Cell Res.*, **13**, 164–171.
23. Wang,H., Vardy,L.A., Tan,C.P., Loo,J.M., Guo,K., Li,J., Lim,S.G., Zhou,J., Chng,W.J., Ng,S.B. *et al.* (2010) PCBP1 suppresses the translation of metastasis-associated PRL-3 phosphatase. *Cancer Cell*, **18**, 52–62.
24. Hanahan,D. and Weinberg,R.A. (2011) Hallmarks of cancer: the next generation. *Cell*, **144**, 646–674.
25. Bartkova,J., Rezaei,N., Liontos,M., Karakaidos,P., Kletsas,D., Issaeva,N., Vassiliou,L.V., Kolettas,E., Niforou,K., Zoumpourlis,V.C. *et al.* (2006) Oncogene-induced senescence is part of the tumorigenesis barrier imposed by DNA damage checkpoints. *Nature*, **444**, 633–637.
26. Gorgoulis,V.G., Vassiliou,L.V., Karakaidos,P., Zacharatos,P., Kotsinas,A., Liloglou,T., Venere,M., Ditullio,R.A. Jr, Kastrinakis,N.G., Levy,B. *et al.* (2005) Activation of the DNA damage checkpoint and genomic instability in human precancerous lesions. *Nature*, **434**, 907–913.
27. Halazonetis,T.D., Gorgoulis,V.G. and Bartek,J. (2008) An oncogene-induced DNA damage model for cancer development. *Science*, **319**, 1352–1355.
28. Pérez-Mancera,P.A., Young,A.R. and Narita,M. (2014) Inside and out: the activities of senescence in cancer. *Nat. Rev. Cancer*, **14**, 547–558.
29. Salama,R., Sadaie,M., Hoare,M. and Narita,M. (2014) Cellular senescence and its effector programs. *Genes Dev.*, **28**, 99–114.

30. Willeit,P., Willeit,J., Kloss-Brandstätter,A., Kronenberg,F. and Kiechl,S. (2011) Fifteen-year follow-up of association between telomere length and incident cancer and cancer mortality. *JAMA*, **306**, 42–44.
31. Doksani,Y. and de Lange,T. (2014) The role of double-strand break repair pathways at functional and dysfunctional telomeres. *Cold Spring Harb. Perspect. Biol.*, **6**, a016576.
32. Sfeir,A. and de Lange,T. (2012) Removal of shelterin reveals the telomere end-protection problem. *Science*, **336**, 593–597.
33. Chen,L.Y., Zhang,Y., Zhang,Q., Li,H., Luo,Z., Fang,H., Kim,SH., Qin,L., Yotnda,P., Xu,J *et al.* (2013) Mitochondrial localization of telomeric protein TIN2 links telomere regulation to metabolic control. *Mol. Cell*, **47**, 839–850.
34. El Maï,M., Wagne,K.D., Michiels,J.F., Ambrosetti,D., Borderie,A., Destree,S., Renault,V., Djerbi,N., Giraud-Panis,M.J., Gilson,E. *et al.* (2014) The telomeric protein TRF2 regulates angiogenesis by binding and activating the PDGFRβ promoter. *Cell Rep.*, **9**, 1047–1060.
35. Teo,H., Ghosh,S., Luesch,H., Ghosh,A., Wong,E.T., Malik,N., Orth,A., de Jesus,P., Perry,A.S., Oliver,J.D. *et al.* (2010) Telomere-independent Rap1 is an IKK adaptor and regulates NF-kappaB-dependent gene expression. *Nat. Cell Biol.*, **12**, 758–767.
36. Yeung,F., Ramírez,C.M., Mateos-Gomez,P.A., Pinzaru,A., Ceccarini,G., Kabir,S., Fernández-Hernando,C. and Sfeir,A. (2013) Nontelomeric role for Rap1 in regulating metabolism and protecting against obesity. *Cell Rep.*, **3**, 1847–1856.
37. Fairall,L., Chapman,L., Moss,H., de Lange,T. and Rhodes,D. (2001) Structure of the TRFH dimerization domain of the human telomeric proteins TRF1 and TRF2. *Mol. Cell*, **8**, 351–361.
38. Doksani,Y., Wu,J.Y., de Lange,T. and Zhuang,X. (2013) Super-resolution fluorescence imaging of telomeres reveals TRF2-dependent T-loop formation. *Cell*, **155**, 345–356.
39. Karlseder,J., Hoke,K., Mirzoeva,O.K., Bakkenist,C., Kastan,M.B., Petrini,J.H. and de Lange,T. (2004) The telomeric protein TRF2 binds the ATM kinase and can inhibit the ATM-dependent DNA damage response. *PLoS Biol.*, **2**, e240.
40. Bae,N.S. and Baumann,P. (2007) A RAP1/TRF2 complex inhibits nonhomologous end-joining at human telomeric DNA ends. *Mol. Cell*, **26**, 323–334.
41. Cesare,A.J., Kaul,Z., Cohen,S.B., Napier,C.E., Pickett,H.A., Neumann,A.A. and Reddel,R.R. (2009) Spontaneous occurrence of telomeric DNA damage response in the absence of chromosome fusions. *Nat. Struct. Mol. Biol.*, **16**, 1244–1251.
42. Hayashi,M.T., Cesare,A.J., Fitzpatrick,J.A., Lazzerini-Denchi,E. and Karlseder,J. (2012) A telomere-dependent DNA damage checkpoint induced by prolonged mitotic arrest. *Nat. Struct. Mol. Biol.*, **19**, 387–394.
43. Rai,R., Zheng,H., He,H., Luo,Y., Multani,A., Carpenter,P.B. and Chang,S. (2010) The function of classical and alternative non-homologous end-joining pathways in the fusion of dysfunctional telomeres. *EMBO J.*, **29**, 2598–2610.
44. Pardo,B. and Marcand,S. (2005) Rap1 prevents telomere fusions by nonhomologous end joining. *EMBO J.*, **24**, 3117–3127.
45. Li,B., Oestreich,S. and de Lange,T. (2000) Identification of human Rap1: implications for telomere evolution. *Cell*, **101**, 471–483.
46. Kabir,S., Hockemeyer,D. and de Lange,T. (2014) TALEN gene knockouts reveal no requirement for the conserved human shelterin protein Rap1 in telomere protection and length regulation. *Cell Rep.*, **9**, 1273–1280.
47. Sarthy,J., Bae,N.S., Scrafford,J. and Baumann,P. (2009) Human RAP1 inhibits non-homologous end joining at telomeres. *EMBO J.*, **28**, 3390–3399.
48. Martinez,P., Thanasoula,M., Carlos,A.R., Gómez-López,G., Tejera,A.M., Schoeftner,S., Dominguez,O., Pisano,D.G., Tarsounas,M. and Blasco,M.A. (2010) Mammalian Rap1 controls telomere function and gene expression through binding to telomeric and extratelomeric sites. *Nat. Cell Biol.*, **12**, 768–780.
49. Sfeir,A., Kabir,S., van Overbeek,M., Celli,G.B. and de Lange,T. (2010) Loss of Rap1 induces telomere recombination in the absence of NHEJ or a DNA damage signal. *Science*, **327**, 1657–1661.
50. Chen,Y., Rai,R., Zhou,Z.R., Kanoh,J., Ribeyre,C., Yang,Y., Zheng,H., Damay,P., Wang,F., Tsujii,H *et al.* (2011) A conserved motif within RAP1 has diversified roles in telomere protection and regulation in different organisms. *Nat. Struct. Mol. Biol.*, **18**, 213–221.
51. Martínez,P., Gómez-López,G., Pisano,D.G., Flores,J.M. and Blasco,M.A. (2016) A genetic interaction between RAP1 and telomerase reveals an unanticipated role for RAP1 in telomere maintenance. *Aging Cell*, **15**, 1113–1125.
52. Rai,R., Chen,Y., Lei,M. and Chang,S. (2016) TRF2-RAP1 is required to protect telomeres from engaging in homologous recombination-mediated deletions and fusions. *Nat. Commun.*, **7**, 10881.
53. Escribano-Díaz,C., Orthwein,A., Fradet-Turcotte,A., Xing,M., Young,J.T., Tkáč,J., Cook,M.A., Rosebrock,A.P., Munro,M., Canny,M.D. *et al.* (2013) A cell cycle-dependent regulatory circuit composed of 53BP1-RIF1 and BRCA1-CtIP controls DNA repair pathway choice. *Mol. Cell*, **49**, 872–883.
54. Roger,L., Jones,R.E., Heppel,N.H., Williams,G.T., Sampson,J.R. and Baird,D.M. (2013) Extensive telomere deprotection in the initiation of colorectal adenomas and its association with chromosomal instability. *J. Natl. Cancer Inst.*, **105**, 1202–1211.
55. Rudolph,K.L., Millard,M., Bosenberg,M.W. and DePinho,R.A. (2001) Telomere dysfunction and evolution of intestinal carcinoma in mice and humans. *Nat. Genet.*, **28**, 155–159.
56. Davoli,T., Denchi,E.L. and de Lange,T. (2010) Persistent telomere damage induces bypass of mitosis and tetraploidy. *Cell*, **141**, 81–93.
57. d'Adda di Fagagna,F., Reaper,P.M., Clay-Farrace,L., Fiegler,H., Carr,P., Von Zglinicki,T., Saretzki,G., Carter,N.P. and Jackson,S.P. (2003) A DNA damage checkpoint response in telomere-initiated senescence. *Nature*, **426**, 194–198.
58. Fumagalli,M., Rossiello,F., Clerici,M., Barozzi,S., Cittaro,D., Kaplunov,J.M., Bucci,G., Dobreva,M., Matti,V., Beausejour,C.M. *et al.* (2012) Telomeric DNA damage is irreparable and causes persistent DNA-damage-response activation. *Nat. Cell Biol.*, **214**, 355–365.
59. Herbig,U., Jobling,W.A., Chen,B.P., Chen,D.J. and Sedivy,J.M. (2004) Telomere shortening triggers senescence of human cells through a pathway involving ATM, p53, and p21(CIP1), but not p16(INK4a). *Mol. Cell*, **14**, 501–513.
60. Feldser,D.M. and Greider,C.W. (2007) Short telomeres limit tumor progression in vivo by inducing senescence. *Cancer Cell*, **11**, 461–469.
61. Guo,X., Deng,Y., Lin,Y., Cosme-Blanco,W., Chan,S., He,H., Yuan,G., Brown,E.J. and Chang,S. (2007) Dysfunctional telomeres activate an ATM-ATR-dependent DNA damage response to suppress tumorigenesis. *EMBO J.*, **26**, 4709–4719.
62. Meena,J.K., Cerutti,A., Beichler,C., Morita,Y., Bruhn,C., Kumar,M., Kraus,J.M., Speicher,M.R., Wang,Z.Q., Kestler,H.A. *et al.* (2015) Telomerase abrogates aneuploidy-induced telomere replication stress, senescence and cell depletion. *EMBO J.*, **34**, 1371–1384.
63. Suram,A., Kaplunov,J., Patel,P.L., Ruan,H., Cerutti,A., Boccardi,V., Fumagalli,M., Di Micco,R., Mirani,N., Gurung,R.L. *et al.* (2012) Oncogene-induced telomere dysfunction enforces cellular senescence in human cancer precursor lesions. *EMBO J.*, **31**, 2839–2851.
64. Loayza,D. and de Lange,T. (2003) POT1 as a terminal transducer of TRF1 telomere length control. *Nature*, **423**, 1013–1018.
65. Lansdorp,P.M., Verwoerd,N.P., van de Rijke,F.M., Dragowska,V., Little,M.T., Dirks,R.W., Raap,A.K. and Tanke,H.J. (1996) Heterogeneity in telomere length of human chromosomes. *Hum. Mol. Genet.*, **5**, 685–691.
66. Bailey,S.M., Meyne,J., Cornforth,M.N., McConnell,T.S. and Goodwin,E.H. (1996) A new method for detecting pericentric inversions using COD-FISH. *Cytogenet. Cell Genet.*, **75**, 48–53.
67. Blasco,M.A., Lee,H.W., Hande,M.P., Samper,E., Lansdorp,P.M., DePinho,R.A. and Greider,C.W. (1997) Telomere shortening and tumor formation by mouse cells lacking telomerase RNA. *Cell*, **91**, 25–34.
68. Callicott,R.J. and Womack,J.E. (2006) Real-time PCR assay for measurement of mouse telomeres. *Comp. Med.*, **56**, 12–22.
69. Cawthon,R.M. (2002) Telomere measurement by quantitative PCR. *Nucleic Acids Res.*, **30**, e47.
70. Xing,X., Peng,L., Qu,L., Ren,T., Dong,B., Su,X. and Shou,C. (2009) Prognostic value of PRL-3 overexpression in early stages of colonic cancer. *Histopathology*, **54**, 309–318.

71. Yang,D., Xiong,Y., Kim,H., He,Q., Li,Y., Chen,R. and Songyang,Z. (2011) Human telomeric proteins occupy selective interstitial sites. *Cell Res.*, **21**, 1013–1027.
72. Zhang,P., Abdelmohsen,K., Liu,Y., Tominaga-Yamanaka,K., Yoon,J.H., Ioannis,G., Martindale,J.L., Zhang,Y., Becker,K.G., Yang,I.H. *et al.* (2015) Novel RNA- and FMRP-binding protein TRF2-S regulates axonal mRNA transport and presynaptic plasticity. *Nat. Commun.*, **6**, 8888.
73. O'Connor,M.S., Safari,A., Liu,D., Qin,J. and Songyang,Z. (2004) The human Rap1 protein complex and modulation of telomere length. *J. Biol. Chem.*, **279**, 28585–28591.
74. Zeng,Q., Si,X., Horstmann,H., Xu,Y., Hong,W. and Pallen,C.J. (2000) Prenylation-dependent association of protein-tyrosine phosphatases PRL-1, -2, and -3 with the plasma membrane and the early endosome. *J. Biol. Chem.*, **275**, 21444–21452.
75. Kirk,K.E., Harmon,B.P., Reichardt,I.K., Sedat,J.W. and Blackburn,E.H. (1997) Block in anaphase chromosome separation caused by a telomerase template mutation. *Science*, **275**, 1478–1481.
76. van Steensel,B., Smogorzewska,A. and de Lange,T. (1998) TRF2 protects human telomeres from end-to-end fusions. *Cell*, **92**, 401–413.
77. Chan,K.L., Palmai-Pallag,T., Ying,S. and Hickson,I.D. (2009) Replication stress induces sister-chromatid bridging at fragile site loci in mitosis. *Nat. Cell Biol.*, **11**, 753–760.
78. Crasta,K., Ganem,N.J., Dagher,R., Lantermann,A.B., Ivanova,E.V., Pan,Y., Nezi,L., Protopopov,A., Chowdhury,D. and Pellman,D. (2012) DNA breaks and chromosome pulverization from errors in mitosis. *Nature*, **482**, 53–58.
79. O'Sullivan,J.N., Bronner,M.P., Brentnall,T.A., Finley,J.C., Shen,W.T., Emerson,S., Emond,M.J., Gollahon,K.A., Moskovitz,A.H., Crispin,D.A *et al.* (2002) Chromosomal instability in ulcerative colitis is related to telomere shortening. *Nat. Genet.*, **32**, 280–284.
80. O'Sullivan,R.J. and Karlseder,J. (2010) Telomeres: protecting chromosomes against genome instability. *Nat. Rev. Mol. Cell Biol.*, **11**, 171–181.
81. Di Micco,R., Sulli,G., Dobreva,M., Liontos,M., Botrugno,O.A., Gargiulo,G., dal Zuffo,R., Matti,V., d'Ario,G., Montani,E. *et al.* (2011) Interplay between oncogene-induced DNA damage response and heterochromatin in senescence and cancer. *Nat. Cell Biol.*, **13**, 292–302.
82. Stewénius,Y., Gorunova,L., Jonson,T., Larsson,N., Höglund,M., Mandahl,N., Mertens,F., Mitelman,F. and Gisselsson,D. (2005) Structural and numerical chromosome changes in colon cancer develop through telomere-mediated anaphase bridges, not through mitotic multipolarity. *Proc. Natl. Acad. Sci. U.S.A.*, **102**, 5541–5546.
83. Callen,E., Di Virgilio,M., Kruhlak,M.J., Nieto-Soler,M., Wong,N., Chen,H.T., Faryabi,R.B., Polato,F., Santos,M., Starnes,L.M. *et al.* (2013) 53BP1 mediates productive and mutagenic DNA repair through distinct phosphoprotein interactions. *Cell*, **153**, 1266–1280.
84. Muñoz,P., Blanco,R., Flores,J.M. and Blasco,M.A. (2005) XPF nuclease-dependent telomere loss and increased DNA damage in mice overexpressing TRF2 result in premature aging and cancer. *Nat. Genet.*, **37**, 1063–1071.
85. Karlseder,J., Smogorzewska,A. and de Lange,T. (2002) Senescence induced by altered telomere state, not telomere loss. *Science*, **295**, 2446–2449.
86. Meira,L.B., Bugni,J.M., Green,S.L., Lee,C.W., Pang,B., Borenshtein,D., Rickman,B.H., Rogers,A.B., Moroski-Erkul,C.A., McFaline,J.L *et al.* (2008) DNA damage induced by chronic inflammation contributes to colon carcinogenesis in mice. *J. Clin. Invest.*, **118**, 2516–2525.
87. Calvo,J.A., Meira,L.B., Lee,C.Y., Moroski-Erkul,C.A., Abolhassani,N., Taghizadeh,K., Eichinger,L.W., Muthupalani,S., Nordstran,L.M., Klungland,A. *et al.* (2012) DNA repair is indispensable for survival after acute inflammation. *J. Clin. Invest.*, **122**, 2680–2689.
88. Jiang,Y., Liu,X.Q., Rajput,A., Geng,L., Ongchin,M., Zeng,Q., Taylor,G.S. and Wang,J. (2011) Phosphatase PRL-3 is a direct regulatory target of TGFbeta in colon cancer metastasis. *Cancer Res.*, **71**, 233–244.
89. Xing,C., Lu,X.X., Guo,P.D., Shen,T., Zhang,S., He,X.S., Gan,W.J., Li,X.M., Wang,J.R., Zhao,Y.Y. *et al.* (2016) Ubiquitin-specific protease 4-mediated deubiquitination and stabilization of PRL-3 is required for potentiating colorectal oncogenesis. *Cancer Res.*, **76**, 83–95.
90. Sabaty,M., Grosse,S., Adryanczyk,G., Boiry,S., Biaso,F., Arnoux,P. and Pignol,D. (2013) Detrimental effect of the 6 His C-terminal tag on YedY enzymatic activity and influence of the TAT signal sequence on YedY synthesis. *BMC Biochem.*, **14**, 28.
91. Noirclerc-Savoye,M., Flayhan,A., Pereira,C., Gallet,B., Gans,P., Ebel,C. and Breyton,C. (2015) Tail proteins of phage T5: investigation of the effect of the His6-tag position, from expression to crystallisation. *Protein Expr. Purif.*, **109**, 70–78.
92. Takai,K.K., Hooper,S., Blackwood,S., Gandhi,R. and de Lange,T. (2010) In vivo stoichiometry of shelterin components. *J. Biol. Chem.*, **285**, 1457–1467.
93. Erdel,F., Kratz,K., Willcox,S., Griffith,J.D., Greene,E.C. and de Lange,T. (2017) Telomere recognition and assembly mechanism of mammalian shelterin. *Cell Rep.*, **18**, 41–53.
94. Stansel,R.M., de Lange,T. and Griffith,J.D. (2001) T-loop assembly in vitro involves binding of TRF2 near the 3' telomeric overhang. *EMBO J.*, **20**, 5532–5540.
95. Yoshimura,S.H., Maruyama,H., Ishikawa,F., Ohki,R. and Takeyasu,K. (2004) Molecular mechanisms of DNA end-loop formation by TRF2. *Genes Cells*, **9**, 205–218.
96. Amiard,S., Doudeau,M., Pinte,S., Poulet,A., Lenain,C., Faivre-Moskalenko,C., Angelov,D., Hug,N., Vindigni,A., Bouvet,P. *et al.* (2007) A topological mechanism for TRF2-enhanced strand invasion. *Nat. Struct. Mol. Biol.*, **14**, 147–154.
97. Arat,N.Ö and Griffith,J.D. (2012) Human Rap1 interacts directly with telomeric DNA and regulates TRF2 localization at the telomere. *J. Biol. Chem.*, **287**, 41583–41594.
98. Gaullier,G., Miron,S., Pisano,S., Buisson,R., Le Bihan,Y.V., Tellier-Lebègue,C., Messaoud,W., Roblin,P., Guimarães,B.G., Thai,R. *et al.* (2016) A higher-order entity formed by the flexible assembly of RAP1 with TRF2. *Nucleic Acids Res.*, **44**, 1962–1976.
99. Pascaru,M., Tanase,C., Vacaru,A.M., Boeti,P., Neagu,E., Popescu,I. and Szedlacsek,S.E. (2009) Analysis of molecular determinants of PRL-3. *J. Cell. Mol. Med.*, **13**, 3141–3150.
100. Janoušková,E., Nečasová,I., Pavloušková,J., Zimmermann,M., Hluchý,M., Marini,V., Nováková,M. and Hofr,C. (2015) Human Rap1 modulates TRF2 attraction to telomeric DNA. *Nucleic Acids Res.*, **43**, 2691–2700.
101. Ye,J.Z., Donigian,J.R., van Overbeek,M., Loayza,D., Luo,Y., Krutchinsky,A.N., Chait,B.T. and de Lange,T. (2004) TIN2 binds TRF1 and TRF2 simultaneously and stabilizes the TRF2 complex on telomeres. *J. Biol. Chem.*, **279**, 47264–47271.
102. Liu,D., O'Connor,M.S., Qin,J. and Songyang,Z. (2004) Telosome, a mammalian telomere-associated complex formed by multiple telomeric proteins. *J. Biol. Chem.*, **279**, 51338–51342.
103. O'Connor,M.S., Safari,A., Xin,H., Liu,D. and Songyang,Z. (2006) A critical role for TPP1 and TIN2 interaction in high-order telomeric complex assembly. *Proc. Natl. Acad. Sci. U.S.A.*, **103**, 11874–11879.
104. Choi,K.H., Farrel,A.S., Lakamp,A.S. and Ouellette,M.M. (2011) Characterization of the DNA binding specificity of Shelterin complexes. *Nucleic Acids Res.*, **39**, 9206–9223.
105. Yang,Q., Zheng,Y.L. and Harris,C.C. (2005) POT1 and TRF2 cooperate to maintain telomeric integrity. *Mol. Cell. Biol.*, **25**, 1070–1080.
106. Hockemeyer,D., Palm,W., Else,T., Daniels,J.P., Takai,K.K., Ye,J.Z., Keegan,C.E., de Lange,T. and Hammer,G.D. (2007) Telomere protection by mammalian Pot1 requires interaction with Tpp1. *Nat. Struct. Mol. Biol.*, **14**, 754–761.
107. Denchi,E.L. and de Lange,T. (2007) Protection of telomeres through independent control of ATM and ATR by TRF2 and POT1. *Nature*, **448**, 1068–1071.
108. Konishi,A. and de Lange,T. (2008) Cell cycle control of telomere protection and NHEJ revealed by a ts mutation in the DNA-binding domain of TRF2. *Genes Dev.*, **22**, 1221–1230.
109. Hockemeyer,D., Daniels,J.P., Takai,H. and de Lange,T. (2006) Recent expansion of the telomeric complex in rodents: two distinct POT1 proteins protect mouse telomeres. *Cell*, **126**, 63–77.
110. Takai,K.K., Kibe,T., Donigian,J.R., Frescas,D. and de Lange,T. (2011) Telomere protection by TPP1/POT1 requires tethering to TIN2. *Mol. Cell*, **44**, 647–659.

111. Rai,R., Li,J.M., Zheng,H., Lok,G.T., Deng,Y., Huen,M.S., Chen,J., Jin,J. and Chang,S. (2011) The E3 ubiquitin ligase Rnf8 stabilizes Tpp1 to promote telomere end protection. *Nat. Struct. Mol. Biol.*, **18**, 1400–1407.
112. Lin,J., Countryman,P., Buncher,N., Kaur,P., E,L., Zhang,Y., Gibson,G., You,C., Watkins,S.C., Piehler,J. *et al.* , (2014) TRF1 and TRF2 use different mechanisms to find telomeric DNA but share a novel mechanism to search for protein partners at telomeres. *Nucleic Acids Res.*, **42**, 2493–2504.
113. Galati,A., Micheli,E., Alicata,C., Ingegnere,T., Cicconi,A., Pusch,M.C., Giraud-Panis,M.J., Gilson,E. and Cacchione,S. (2015) TRF1 and TRF2 binding to telomeres is modulated by nucleosomal organization. *Nucleic Acids Res.*, **43**, 5824–5837.
114. Oikawa,S., Tada-Oikawa,S. and Kawanishi,S. (2001) Site-specific DNA damage at the GGG sequence by UVA involves acceleration of telomere shortening. *Biochemistry*, **40**, 4763–4768.
115. Sun,L., Tan,R., Xu,J., LaFace,J., Gao,Y., Xiao,Y., Attar,M., Neumann,C., Li,G.M., Su,B. *et al.* , (2015) Targeted DNA damage at individual telomeres disrupts their integrity and triggers cell death. *Nucleic Acids Res.*, **43**, 6334–6347.
116. Hewitt,G., Jurk,D., Marques,F.D., Correia-Melo,C., Hardy,T., Gackowska,A., Anderson,R., Taschuk,M., Mann,J. and Passos,J.F. (2012) Telomeres are favoured targets of a persistent DNA damage response in ageing and stress-induced senescence. *Nat. Commun.*, **3**, 708.
117. Opresko,P.L., Fan,J., Danzy,S., Wilson,D.M 3rd and Bohr,V.A. (2005) Oxidative damage in telomeric DNA disrupts recognition by TRF1 and TRF2. *Nucleic Acids Res.*, **33**, 1230–1239.